Summer 7-18-2019

A Multi-Sensor Phenotyping System: Applications on Wheat Height Estimation and Soybean Trait Early Prediction

Wenan Yuan
University of Nebraska - Lincoln, wenan.yuan@huskers.unl.edu

A MULTI-SENSOR PHENOTYPING SYSTEM: APPLICATIONS ON WHEAT HEIGHT ESTIMATION AND SOYBEAN TRAIT EARLY PREDICTION

by

Wenan Yuan

A THESIS

Presented to the Faculty of

The Graduate College at the University of Nebraska

In Partial Fulfilment of Requirements

For the Degree of Master of Science

Major: Agricultural and Biological Systems Engineering

Under the Supervision of Professor Yufeng Ge

Lincoln, Nebraska

August, 2019

A MULTI-SENSOR PHENOTYPING SYSTEM: APPLICATIONS ON WHEAT HEIGHT ESTIMATION AND SOYBEAN TRAIT EARLY PREDICTION

Wenan Yuan, M.S.

University of Nebraska, 2019

Advisor: Yufeng Ge

Phenotyping is an essential aspect for plant breeding research since it is the foundation of the plant selection process. Traditional plant phenotyping methods such as measuring and recording plant traits manually can be inefficient, laborious and prone to error. With the help of modern sensing technologies, high-throughput field phenotyping is becoming popular recently due to its ability of sensing various crop traits non-destructively with high efficiency. A multi-sensor phenotyping system equipped with red-green-blue (RGB) cameras, radiometers, ultrasonic sensors, spectrometers, a global positioning system (GPS) receiver, a pyranometer, a temperature and relative humidity probe and a light detection and ranging (LiDAR) was first constructed, and a LabVIEW program was developed for sensor controlling and data acquisition. Two studies were conducted focusing on system performance examination and data exploration respectively. The first study was to compare wheat height measurements from ultrasonic sensor and LiDAR. Canopy heights of 100 wheat plots were estimated five times over the season by the ground phenotyping system, and the results were compared to manual measurements. Overall, LiDAR provided the better estimations with root mean square error (RMSE) of 0.05 m and R^2 of 0.97. Ultrasonic sensor did not perform well due to the style of our application. In conclusion LiDAR was recommended as a reliable method for

wheat height evaluation. The second study was to explore the possibility of early predicting soybean traits through color and texture features of canopy images. Six thousand three hundred and eighty-three RGB images were captured at V4/V5 growth stage over 5667 soybean plots growing at four locations. One hundred and forty color features and 315 gray-level co-occurrence matrix (GLCM)-based texture features were derived from each image. Another two variables were also introduced to account for the location and timing difference between images. Cubist and Random Forests were used for regression and classification modelling respectively. Yield (RMSE=9.82, R^2=0.68), Maturity (RMSE=3.70, R^2=0.76) and Seed Size (RMSE=1.63, R^2=0.53) were identified as potential soybean traits that might be early-predictable.

ACKNOWLEDGMENTS

I would like to thank my advisor Dr. Yufeng Ge for offering me this great learning and research opportunity as well as his academic guidance and financial support throughout my master's program.

I am honored to have Dr. Yufeng Ge, Dr. George Meyer and Dr. P. Stephen Baenziger serving as my committee members.

I would like to thank my colleagues Dr. Geng Bai, Abbas Atefi, Nuwan Kumara Wijewardane, Suresh Thapa, Piyush Pandey, Ujjwol Bhandari, Jiating Li and Arun Narenthiran Veeranampalayam Sivakumar for helping with my difficulties in research and life.

I would like to thank Dr. Geng Bai, Shawn Jenkins, Jiating Li, Madhav Bhatta, Dr. Yeyin Shi, Dr. P. Stephen Baenziger, Dr. George L. Graef and Dr. Yufeng Ge for making my publications possible.

I would like to thank Dr. Geng Bai, Ujjwol Bhandari, Bo Zhang, Yanni Yang, Arena Ezzati See and Hao Zhang for helping me with the field activities.

I would like to thank Scott Minchow for helping me make all the devices used in my projects.

I would like to thank all the instructors of the classes that I have taken at UNL for teaching me the knowledge.

Thank everyone for being part of my journey.

TABLE OF CONTENTS

LIST OF TABLES

LIST OF FIGURES

LIST OF EQUATIONS

CHAPTER 1

INTRODUCTION

1.1. Importance of High-Throughput Field Phenotyping

Genotype refers to the genetic makeup of an organism, which in a large degree determines the organism's characteristics. However, genotype itself is not the only factor that would influence gene expression. Environment, or the living conditions of an organism, also plays a big role in shaping its final appearance. Hence, the term phenotype was created, meaning the set of observable characteristics of an organism resulting from the interaction of its genotype with the environment. In agriculture, plant phenotyping aims to quantitatively describe the morphological, physiological and biochemical properties of a plant (Walter, Liebisch, and Hund 2015), which can have a significant implication for plant breeding in terms of helping understand gene expression under certain environments.

Plant breeding has long been a key method for improving the quality of agricultural products in human history, and one of its fundamentals is plant selection based on plant phenotypes. Since the beginning of domestication to Gregor Mendel's experiments with pea plant hybridization, plant propagation is more or less dependent on plant phenotyping as newly developed varieties need to be assessed based on certain plant parameters such as yield. The process of quantifying plant traits in a standardized manner is the essence of plant phenotyping, and the quantified plant traits allow breeders to compare different plant varieties and make selections.

Modern biotechnologies such as marker-assisted selection and low-cost DNA sequencing have greatly improved the efficiency of genomic research (Behjati and Tarpey 2013), while traditional plant phenotyping in field is not able to keep up with the pace due to its disadvantage of being laborious and inefficient. Humans are typically heavily involved in traditional plant phenotyping activities, such as destructive sampling, visual estimation, or physical measurement of experimental plots. Yet it is challenging to perform those procedures on thousands of plots. Many considered high-throughput field phenotyping as a bottleneck for both conventional and modern plant breeding (Araus et al. 2018; Underwood et al. 2017), and this challenge stands in the way of the next green revolution (Bai et al. 2016), which would be essential for future global food security by 2050 (Ray et al. 2012).

1.2. Existing Multi-Sensor Phenotyping Systems

Diverse approaches for field phenotyping exist. From hand-held devices, fixed in-field sensors, to mobile airborne or ground platforms, each has their unique advantages and limitations (Deery et al. 2014). For example, fixed systems can only monitor limited amount of plots, but they are usually fully automated and can provide measurements in high quality. Airborne platforms such as unmanned aircraft vehicles have limited payload, however they have high data collection efficiency and are not limited by geography. Ground mobiles, on the other hand, can differ from each other greatly in terms of cost, payload, and sensing modules. Generally speaking ground platforms have high payloads and are more flexible in terms of the measuring area, however they tend to be less efficient than airborne platforms.

Ground-based multi-sensor phenotyping systems have been gaining popularity in recent years due to their ability of sensing various crop traits non-destructively in a high-throughput fashion, and efforts have been made by researchers and engineers on developing sophisticated systems in the past. The following are some examples of such systems:

• BreedVision

BreedVision was a tractor-pulled phenotyping platform for small grain cereals (Busemeyer et al. 2013). It was equipped with laser distance sensors, light curtains, time-of-flight cameras, a hyperspectral camera, RGB cameras, a GPS receiver and a rotary encoder (Figure 1.1).

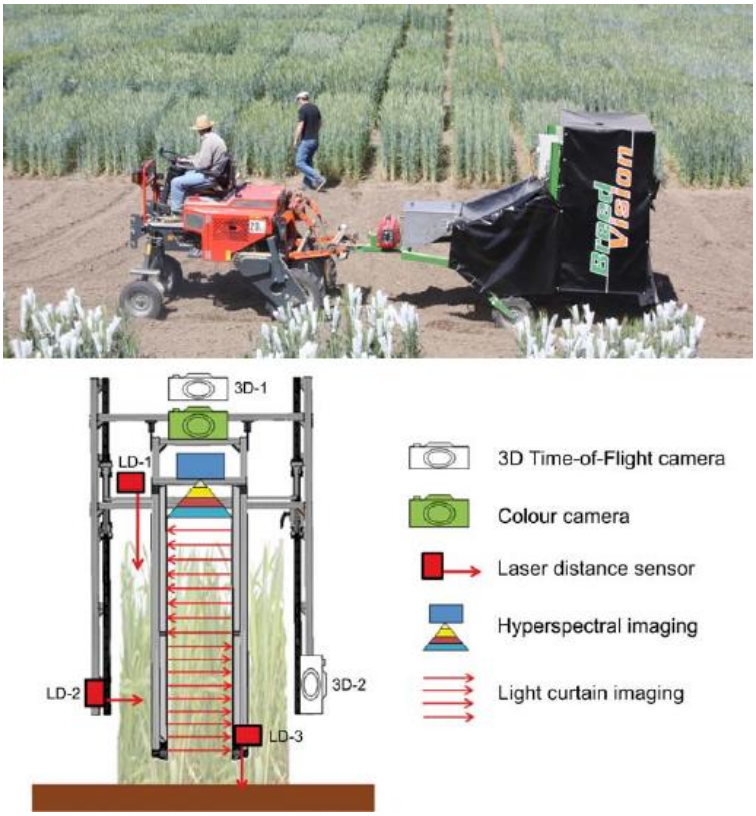

Figure 1.1. BreedVision platform and sensor layout (Busemeyer et al. 2013).

Based on just a single sensor or the fusion of multiple sensors, the platform can be used for determining simple or complex crop parameters such as plant height, plant moisture content, tiller density and dry biomass yield.

• Maricopa Phenotyping System

A tractor-based multi-sensor system was developed for phenotyping plant dynamic traits and tested in 2011 in Maricopa, Arizona (Andrade-Sanchez et al. 2014). The system carried a GPS receiver and four sets of sensors consisting of a sonar proximity sensor, an infrared radiometer and a multispectral crop canopy sensor (Figure 1.2).

Figure 1.2. The Maricopa phenotyping system: (a) front view; (b) the sonar proximity sensor; (c) the infrared radiometer; (d) the GPS receiver; (e) the multispectral crop canopy sensor (Andrade-Sanchez et al. 2014).

Canopy height, canopy temperature and normalized difference vegetation index (NDVI) of four experimental plots can be measured simultaneously, which all showed differences between cultivars in the study.

• Phenomobile

Deery et al. (2014) reported a buggy for plant phenotyping purposes. The mobile was installed with wheel encoders, a GPS receiver, LiDARs, RGB cameras, a thermal infrared camera, infrared thermometers, a spectrometer and a hyperspectral line scanner camera (Figure 1.3).

	Description
1	Frame with 1.5 m ground clearance
2	Wheel encoders (~1-mm accuracy)
3	Real time kinematic GPS (~2-cm accuracy)
4	Height adjustable boom (max 3 m)
5	Removable light bank
6	Three LiDAR sensors
7	Four RGB stereo cameras
8	Spectrometer/ hyperspectral camera
9	Infra-red thermometers/ infra-red thermal camera
10	Generator and electronics
11	Two wheel drive hydraulic drive system

Figure 1.3. Phenomobile and its sensor components (Deery et al. 2014).

In the study the possible uses of each sensor component of Phenomobile were explained in details. LiDAR signals are able to show the high contrast betwee soil and vegetation, from which ground cover and possibly plant seedling counts might be evaluated. Aside from basic plant height information, LiDAR's high resolution data could also be used for estimating advanced canopy structural parameters such as leaf

angular distribution. RGB cameras were used for assessing leaf area and volume based on stereo vision algorithm in the study. By moving the mobile slowly, high resolution data could be collected from the hyperspectral camera and the spectrometer, and it was possible to extract the reflectance information from individual plants and distinguish between individual plant organs such as flag leaves and spikes. Spectral vegetation indices could also be calculated to estimate plant parameters such as leaf area index, nutrient contents and water status. Thermal infrared camera was used to assessing canopy temperatures, which could be an indicator for overall canopy transpiration.

• Ladybird

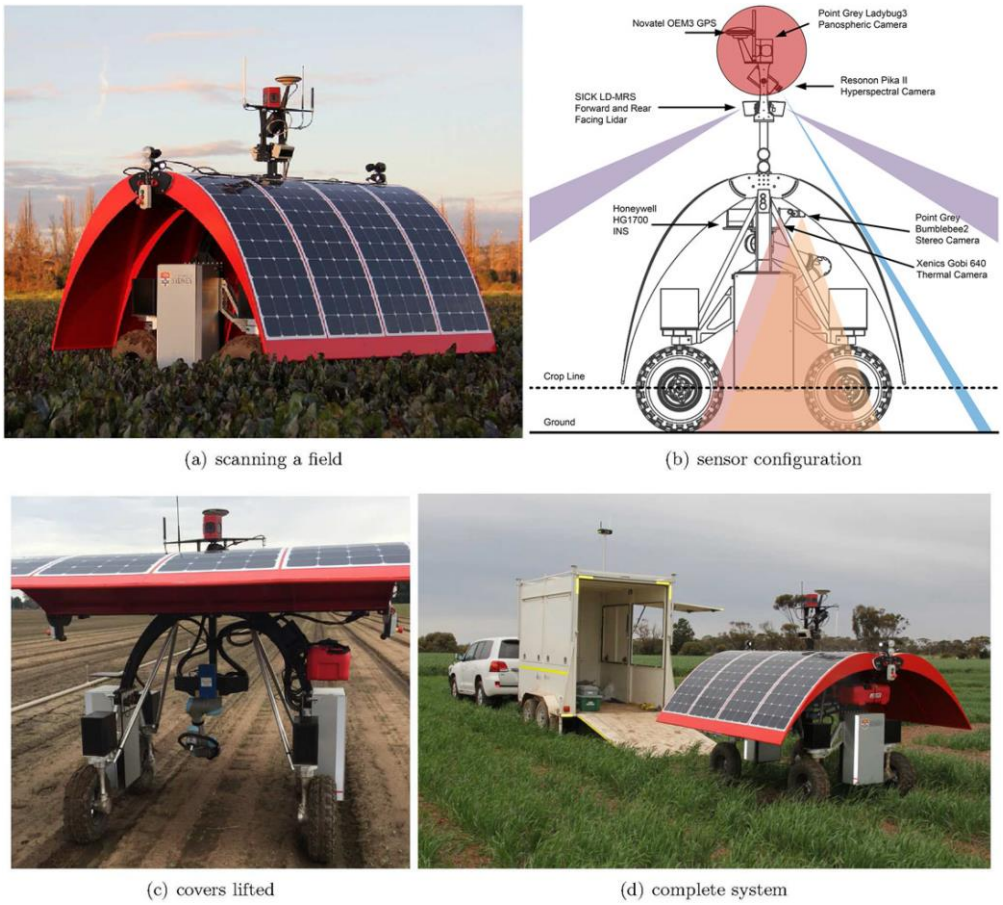

Figure 1.4. Ladybird robot and its sensor configurations (Underwood et al. 2017).

Ladybird was an autonomous unmanned ground-vehicle robot for row-crop phenotyping (Underwood et al. 2017), which was also coupled with a data processing framework. The robot is equipped with a GPS receiver and an inertial navigation systems (INS) receiver, forward and rear facing LiDARs, a panospheric camera, a hyperspectral camera, a stereo camera and a thermal camera (Figure 1.4).

Underwood et al. (2017) only reported the application of LiDAR and hyperspectral camera of the system, and three key crop traits were observed. LiDAR was utilized for crop height measurement since height influences harvest index and lodging risk, and hyperspectral camera was used for NDVI and canopy closure measurements, which are related with chlorophyll and nitrogen concentration, and humidity driven diseases respectively.

• Field Scanalyzer

Field Scanalyzer was a fixed site, fully automated robotic phenotyping platform installed at Rothamsted Research, England (Virlet et al. 2017). The system has a camera box, within which multiple sensors were mounted: a visible camera, a thermal infrared camera, 3D laser scanners, a visible and near-infrared camera and an extended visible and near-infrared camera, a NDVI sensor and a chlorophyll fluorescence imager (Figure 1.5).

The actual usage of each sensor component of the system were not described explicitly in the study, however the authors mentioned some potential sensor applications. RGB camera of the system could be used for monitoring canopy closure, by segmenting plants from soil and calculating the percentage of green pixels of an image. Also it could be used to monitor canopy development overtime and detect and quantify

plant organs such as wheat ears. Thermal infrared camera could provide plant temperature information, which can further be used to assess crop water status. Plant heights could be derived from laser scanner's point cloud images. Chlorophyll fluorescence imager could help simplify the task of quantifying plant photosynthetic capacity in field at night. The entire spectrum of hyperspectral data could be utilized through multivariate approaches to predict early biotic stress, and plant nitrogen and water content.

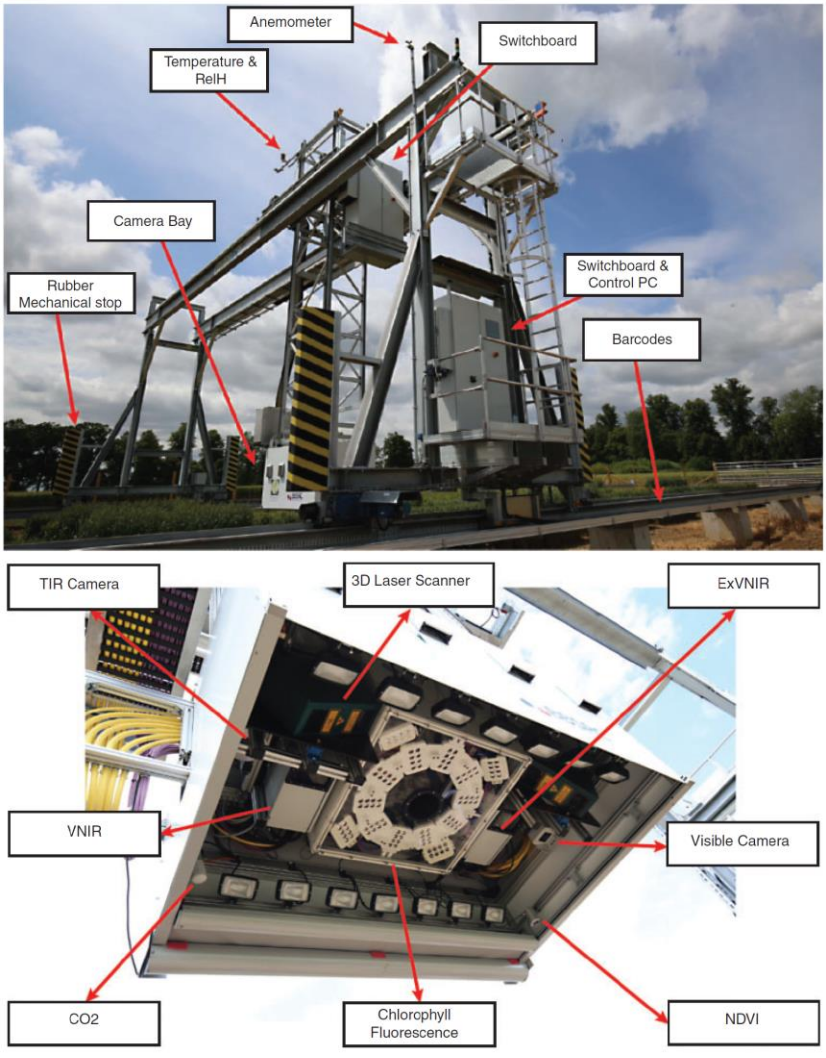

Figure 1.5. Field Scanalyzer and its camera box (Virlet et al. 2017).

• Phenomobile Lite

Phenomobile Lite was a dedicated plant phenotyping mobile with aluminum frame, electric motor and adjustable wheelbase to accommodate for various plot width (Jimenez-Berni et al. 2018). It comprised of a LiDAR, an INS receiver and a GPS receiver and an incremental wheel encoder. The system was also able to integrate other sensors such as active NDVI sensor and digital camera (Figure 1.6). In the study three plant traits were extracted from LiDAR data, namely canopy height, ground cover and above-ground biomass.

Figure 1.6. Phenomobile Lite and its sensor components (Jimenez-Berni et al. 2018).

1.3. Objectives

The primary objective of this thesis was to develop a fully functioning ground-based multi-sensor plant phenotyping system. Two follow-up studies were conducted respectively: the first study was to examine the system's performance on wheat height estimation; the second study was to explore a new methodology of utilizing RGB images to early predict soybean traits.

CHAPTER 2

DEVELOPMENT OF THE MULTI-SENSOR PHENOTYPING SYSTEM

2.1. Hardware

2.1.1. Sensors

Eight types of sensors were selected for the system in order to measure various crop traits and environmental conditions. As an overview, sensor models and manufacturers, total amounts of sensors employed in the system, sensor input voltage requirements and meanings of sensor measurements were listed in Table 2.1.

Table 2.1. Sensor overview of the phenotyping system.

Sensor Model	Manufacturer	Amount	Voltage	Measurement
HD Webcam C270	Logitech, Lausanne, Switzerland	Three	USB	Canopy RGB image
SI-131 Infrared Radiometer	Apogee Instruments, Inc., Logan, UT, USA	Three	2.5 V	Canopy temperature
ToughSonic 14 Ultrasonic Sensor	Senix Corporation, Hinesburg, VT, USA	Three	10 - 30 V	Canopy height
VLP-16 Puck LiDAR	Velodyne LiDAR, Inc., San Jose, CA, USA	One	12 V	Canopy 3D point cloud
Flame-S-VIS-NIR Spectrometer	Ocean Optics, Inc., Largo, FL, USA	Four	USB	Canopy spectral reflectance, incoming radiation spectrum
SP-110 Pyranometer	Apogee Instruments, Inc., Logan, UT, USA	One	Self-powered	Incoming shortwave radiation

HMP60 Temperature and Relative Humidity Probe	Campbell Scientific, Inc., Logan, UT, USA	One	5 - 28 V	Air temperature, relative humidity
AgGPS 162 Receiver	Trimble Inc, Sunnyvale, CA, USA	One	10 - 16 V	Plot location

Key sensor specifications and common applications of sensor measurements in field phenotyping were summarized below:

• HD Webcam C270

The webcam uses USB 2.0 for data communication. It has a fixed focus, a 60° diagonal field of view (FOV) and a 1280×960 optical resolution. RGB images contain information regarding plant color and morphology. Estimating plant canopy cover through plant segmentation is a typical usage of RGB images. Vegetation indices based on R, G and B bands can be derived for assessment of plant parameters such as chlorophyll content (Hunt et al. 2013). Plant 3D canopy structure can also be generated from 2D images using structure from motion (Wilke et al. 2019) or other techniques.

• SI-131 Infrared Radiometer

The radiometer consists of an internal thermistor and a thermopile and it measures temperature based on the Stefan-Boltzmann Law. The thermistor measures the sensor body temperature. It requires a 2.5 V excitation voltage, and typically produces 0 to 2500 mV single-ended signals. The self-powered thermopile measures the infrared radiation emitted or reflected by the target. It has a FOV of 28°, gives approximately -1.1 to 1.1 V differential signals for targets with temperatures ranging from -55 to 55 °C. Along with

other parameters such as air temperature, canopy temperature can be used for indicating plant water stress (Jackson, Reginato, and Idso 1977) and assessing plant heat and drought tolerance (Balota et al. 2007).

• ToughSonic 14 Ultrasonic Sensor

The ultrasonic sensor has a total FOV of 14°, and it measures distance from 4 in to 168 in with a resolution of 0.0034 in. The sensor produces 0 to 10 V single-ended signals. Plant height is an important parameter when it comes to plant genotype selection in breeding programs. Besides for plant height, ultrasonic sensors have also been applied for plant biomass estimation (Fricke, Richter, and Wachendorf 2011; Pittman et al. 2015) and weed detection (Andújar, Weis, and Gerhards 2012).

• VLP-16 Puck LiDAR

The LiDAR transfers data via Ethernet. It has 16 near-infrared lasers with a 903 nm wavelength, and it detects distance up to 100 m. The sensor has a vertical FOV of 30° with a resolution of 2°, and a horizontal FOV of 360° with an adjustable resolution between 0.1° and 0.4° (Yuan et al. 2018). Plant 3D point cloud can be used for extracting multiple plant parameters such as height, ground cover, biomass (Jimenez-Berni et al. 2018), leaf area index and plant area density (Deery et al. 2014).

• Flame-S-VIS-NIR Spectrometer

The spectrometer uses USB 2.0 for transferring data. It detects light within the spectral range of 350 to 1000 nm at a 0.1 to 10 nm resolution. The integration time can be set from 1 ms to 65 s. The optical fiber coupled with the spectrometer has a FOV of

25.4°. Various vegetation indices such as NDVI can be derived from canopy spectral reflectance and used for assessing vegetation cover, vigor, and growth dynamics (Xue and Su 2017). Due to the limited FOV, spectrometers are not the most practical instrument for field phenotyping, whereas hyperspectral cameras are gradually becoming the mainstream (Xu, Li, and Paterson 2019).

• SP-110 Pyranometer

The pyranometer has a FOV of 180° and measures solar radiation within the spectral range of 360 to 1120 nm. It generates 0 to 350 mV differential signals. Solar radiation can be used for estimating evapotranspiration and predicting infection risk of fungal diseases, thus is informative for scheduling irrigation and fungicide spraying (López-Lapeña and Pallas-Areny 2018).

• HMP60 Temperature and Relative Humidity Probe

The probe measures temperature from -40 to 60 °C and relative humidity from 0 to 100%. It produces two 0 to 1 V single-ended signals. The difference between air temperature and canopy temperature is typically calculated as an indicator for plant water status as mentioned above. Similarly, along with dry bulb air temperature and net radiation, wet bulb air temperature can be estimated from relative humidity and crop water stress index can be calculated (Jackson et al. 1981), which is useful for facilitating irrigation scheduling.

• AgGPS 162 Receiver

The GPS receiver has a pass-to-pass accuracy of ±8 to 12 in, and it uses RS-232

for data communication. The location information of plants helps match phenotypic data with agronomic data, and the unwanted spatial variability in data can be accounted during data analysis (Stroup, Baenziger, and Mulitze 1994). GPS coordinates are also commonly needed for data mapping of certain instruments such as LiDAR.

2.1.2. Hardware Connection

A data acquisition (DAQ) device LabJack U6 with one Mux80 AIN Expansion Board and one CB37 Terminal Board (LabJack Corporation, Lakewood, CO, USA) was used for reading sensor voltage signals. A 10-Port Industrial USB 3.0 Hub (StarTech.com, Lockbourne, OH) was used for receiving USB signals. Figure 2.1 shows the data communications between different hardware components.

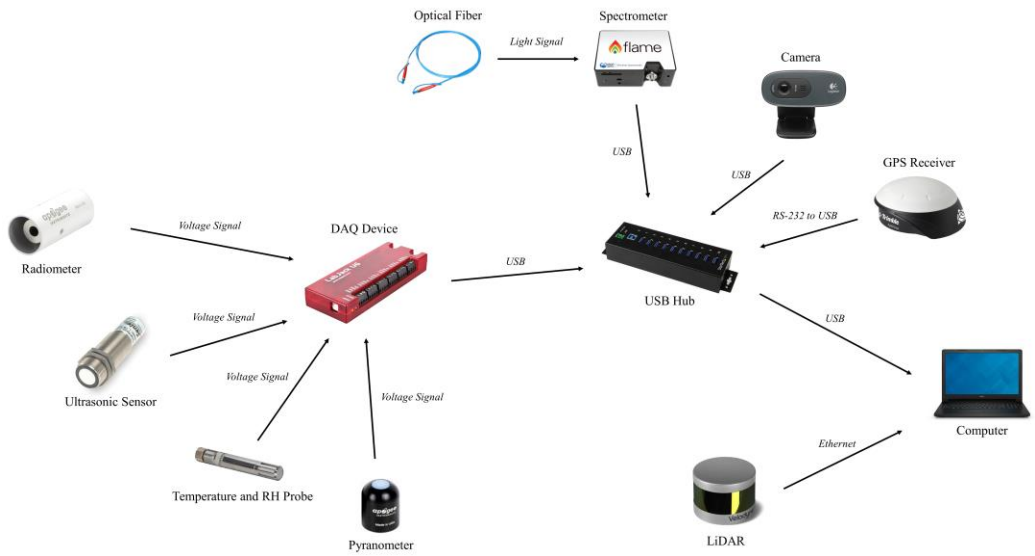

Figure 2.1. Flowchart of data communications between sensors and computer of the phenotyping system.

All hardware components are either installed on “sensor bars” or placed in the “DAQ box”. There are three down-looking sensor bars allowing the system scanning

three plots simultaneously, and one up-looking sensor bar for monitoring the environment (Figure 2.2). Except for LiDAR, three down-looking sensor bars have identical sensor arrangements.

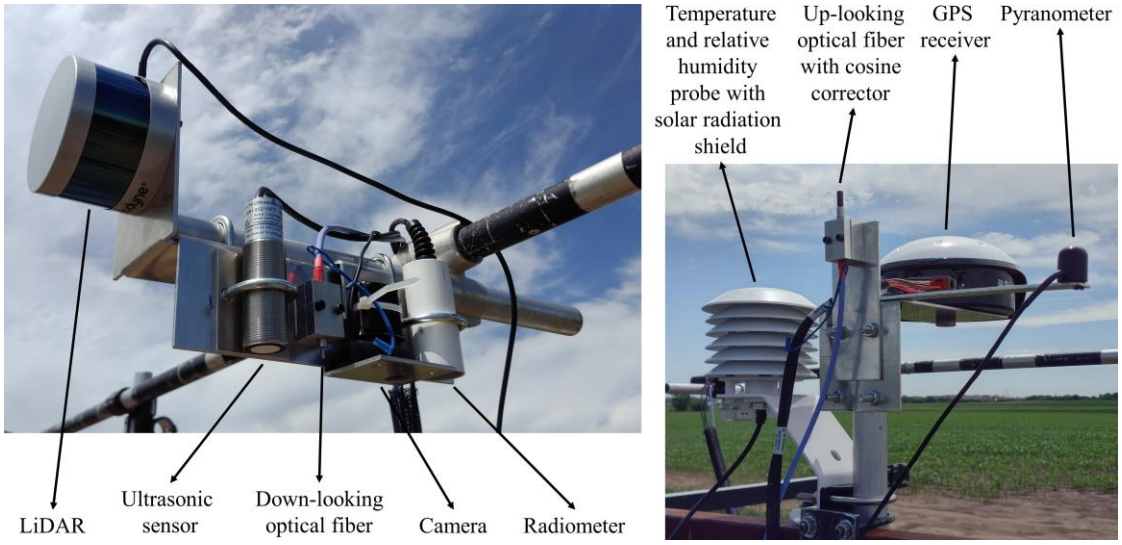

Figure 2.2. Down-looking and up-looking sensor bar of the phenotyping system.

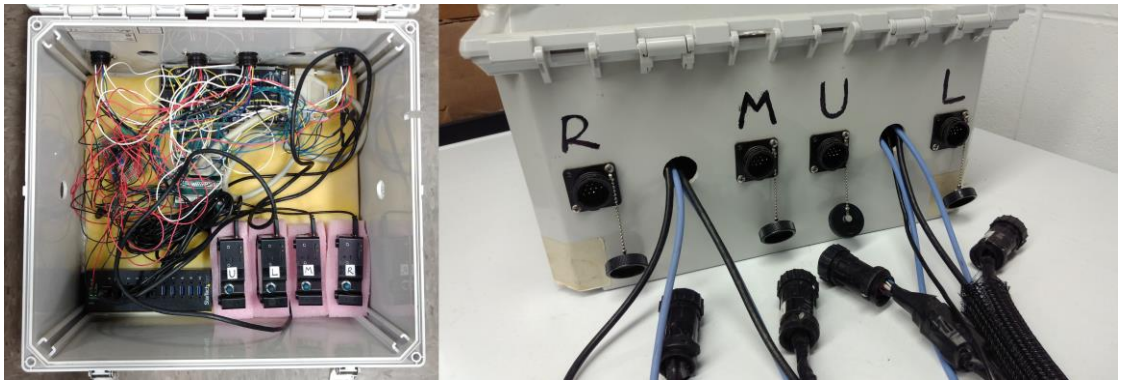

Figure 2.3. Inside and outside of the DAQ box of the phenotyping system.

A power supply circuit, the DAQ device, the USB hub and four spectrometers are placed in the DAQ box (Figure 2.3). Sensor USB cables and optical fibers can be directly plugged inside the box, while sensor signal and power wires connect to the box through circular connectors (Figure 2.3).

The carrier of the phenotyping system, “phenocart”, which consists of two bicycles, a metal platform and a metal frame, was developed by Bai et al. (2016) (Figure 2.4). Sensor bars can be mounted to the frame through pipefittings, and batteries, DAQ box and computer can be placed on the platform. The phenocart has a clearance of 4 ft, and the wheel spacing between two bicycles is 60 in. The cart can be operated by one or two people using the bicycle handlebars.

Figure 2.4. The assembled phenotyping system.

2.2. Software

2.2.1. Functions

A customized software was developed for sensor controlling and data acquisition using LabVIEW 2016 (National Instruments, Austin, TX, USA) (Figure 2.5). A static measurement style was adopted for the system. Instead of collecting data continuously, sensor outputs were saved only when designated buttons were triggered.

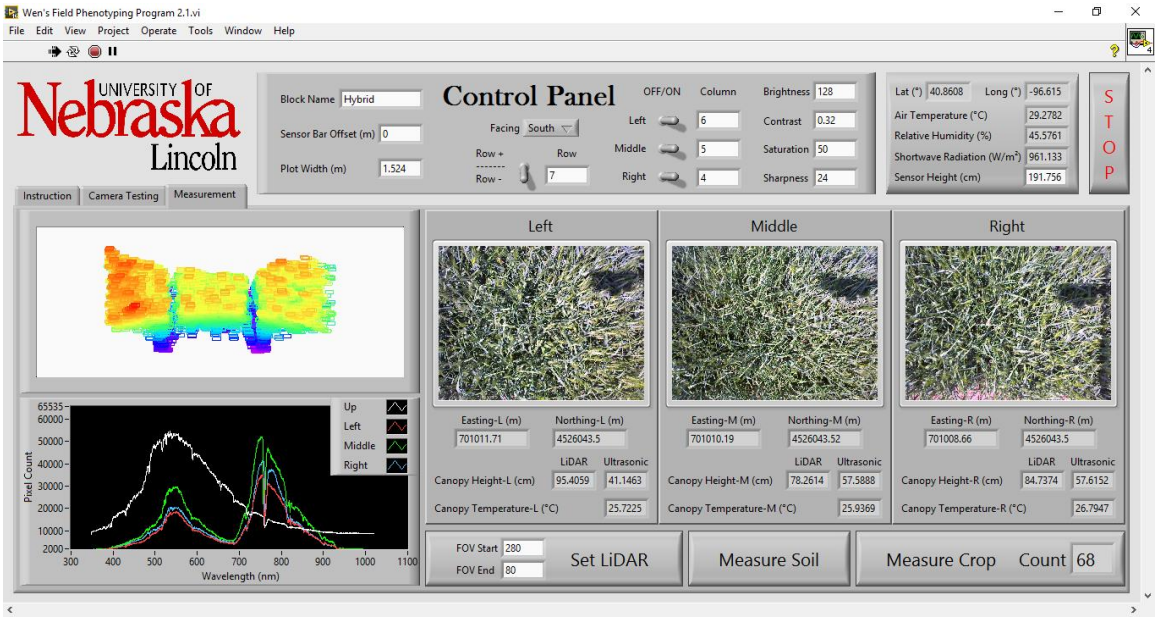

Figure 2.5. Front panel of the LabVIEW program.

The main functions of the software include the following:

• Allowing users to input Row and Column identification numbers for the plots being scanned if such numbers have been pre-assigned;

• Allowing users to turn on or off data saving for any of the three down-looking sensor bars;

• Allowing users to adjust four camera attributes including brightness, contrast, saturation and sharpness;

• Allowing users to set starting and ending position of LiDAR's horizontal FOV;

• Displaying real-time point cloud of three plots being scanned by LiDAR, and saving point cloud data to csv files when measured;

• Displaying real-time incoming radiation spectrum and three canopy reflectance

spectra with automatic integration time, and saving spectrum data to csv files when measured;

• Displaying real-time GPS coordinates of the cart, air temperature, relative humidity and total incoming shortwave radiation of the environment, canopy temperatures and canopy heights estimated from both ultrasonic sensor and LiDAR for three plots being scanned, and saving the readings to one csv file;

• Displaying images of crop canopies captured by the cameras, and saving images as png files.

2.2.2. Programming

Five major dataflow components existed (Figure 2.6). Built-in LabVIEW virtual instruments (VIs) under “VISA” function palette were used for reading serial port signals from the GPS receiver. Publicly available VIs “LabVIEW_LJUD” were used for reading the voltage signals from the DAQ device’s analog inputs. VIs “Ocean Optics 2000 4000” from Instrument Driver Network of National Instruments were used for calculating the sampling wavelengths of each spectrometer and reading the spectrum signals. Built-in VIs under “NI-IMAQdx” function palette were used for capturing images through the cameras and saving the images. A customized subVI was created for communicating with LiDAR (Figure 2.7), and details can be found in Chapter 3.2.2.

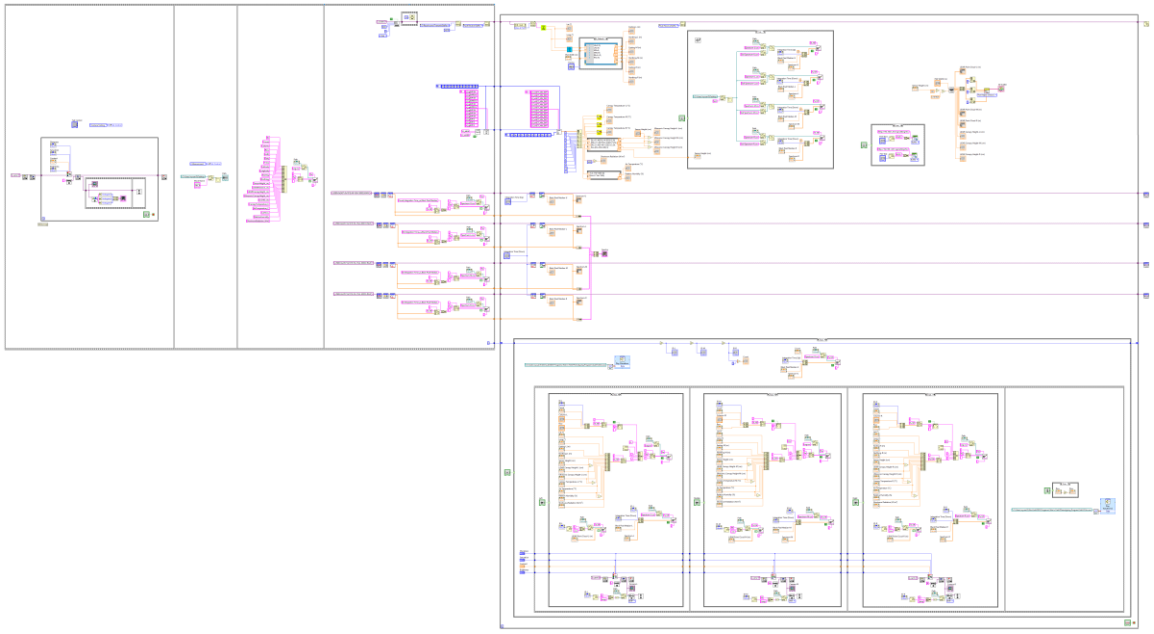

Figure 2.6. Block diagram of the LabVIEW program.

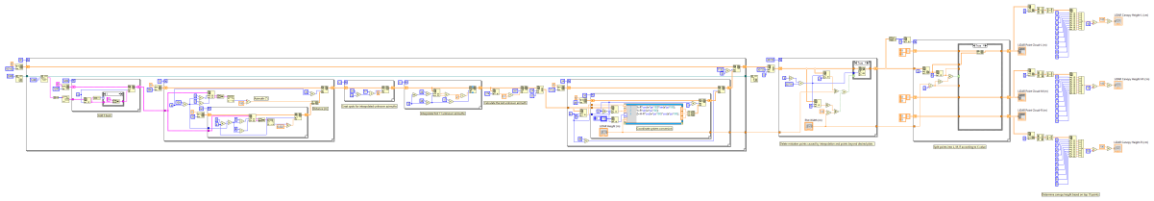

Figure 2.7. Block diagram of the LiDAR subVI.

Figure 2.8 shows the basic programming logic of the software. A while loop is used for keeping the program refreshing the sensor readings, which runs once per second. Inside the while loop, a case structure, which examines whether the “Measure” button is triggered or not, is responsible for saving the sensor readings.

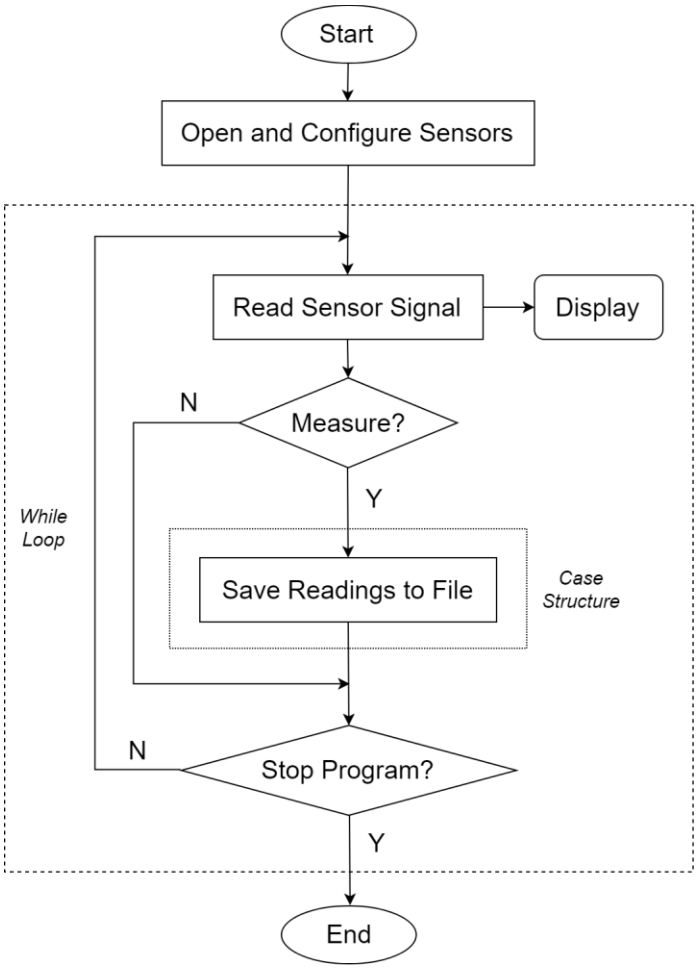

Figure 2.8. Programming logic flowchart of the LabVIEW program.

CHAPTER 3

WHEAT HEIGHT ESTIMATION USING ULTRASONIC SENSOR AND LIDAR[1]

3.1. Background

Plant height is one of the most important parameters for crop selection in breeding programs. For wheat, height is associated with grain yield (Bhatta et al. 2017), lodging (Navabi et al. 2006), biomass (Schirrmann et al. 2016), and resistance to certain disease (Mao et al. 2010). Traditionally plant height is measured manually using a yardstick. This method is labor-intensive and time-consuming when a large number of plants need to be evaluated. In addition, it is prone to error during reading and recording, especially in harsh weather conditions. Alternative but reliable methods for plant height evaluation are needed.

As some of the most common methods for plant height estimation nowadays, ultrasonic sensor and LiDAR are favored over one another because of the unique advantages and disadvantages they possess. Ultrasonic sensor is typically inexpensive and user-friendly, and it has a long history of being utilized in plant height measurement (Fricke et al. 2011). However some of its disadvantages include reduced sensor accuracies when sensors become farther from objects due to the larger FOV (Sun, Li, and Paterson 2017), sensor's sensitivity to temperature as sound speed changes with temperature (Barker et al. 2016), and the susceptibility of sound waves to plant leaf size,

[1] This chapter is a portion of a published journal article: Yuan, W., Li, J., Bhatta, M., Shi, Y., Baenziger, P. S., & Ge, Y. (2018). Wheat Height Estimation Using LiDAR in Comparison to Ultrasonic Sensor and UAS. *Sensors*, 18(11).

angle, and surfaces (Fricke et al. 2011). LiDAR is a relatively new methods for estimating various plant traits such as height, biomass and ground cover (Jimenez-Berni et al. 2018). LiDAR is considered as a widely-accepted and promising sensor for plant 3D reconstruction because of its high spatial resolution, low beam divergence and versatility regardless of ambient light conditions (Jimenez-Berni et al. 2018; Shi et al. 2015; Underwood et al. 2017). Yet, LiDAR is also costly, and LiDAR data can be voluminous and challenging to process.

Ultrasonic sensor and LiDAR have been both exploited for a wide range of crops in the past. However, ultrasonic sensor was not able to provide consistently accurate height estimations when compared to LiDAR. For example, ultrasonic sensor has been used to estimate the height of cotton (Andrade-Sanchez et al. 2014; Sharma and Ritchie 2015), alfalfa (Pittman et al. 2015), wild blueberry (Chang et al. 2017; Farooque et al. 2013), legume-grass mixture (Fricke et al. 2011; Fricke and Wachendorf 2013), bermudagrass (Pittman et al. 2015), barley (Barmeier, Mistele, and Schmidhalter 2016) and wheat (Andújar et al. 2012; Pittman et al. 2015; Scotford and Miller 2004), and RMSE from 0.022 to 0.072 m and R^2 from 0.44 to 0.90 were observed. On the other hand, LiDAR has been employed for crops such as cotton (Sun et al. 2017), blueberry (Sun and Li 2016) and wheat (Deery et al. 2014; Friedli et al. 2016; Jimenez-Berni et al. 2018; Madec et al. 2017; Underwood et al. 2017; Virlet et al. 2017), and RMSE from 0.017 to 0.089 m and R^2 from 0.86 to 0.99 were obtained.

In existing studies of utilizing terrestrial LiDAR, an experimental field is usually scanned by a LiDAR that moves continuously with a constant speed. For a manned multi-

sensor system, this might be problematic since sensors such as cameras often require to be stationary to record high quality data, which can cause difficulties for software programming to harness multiple sensor dataflows simultaneously, as well as actual system operating for maintaining the uniform speed. Moreover, despite all the successes and failures of applying ultrasonic sensor and LiDAR in plant height estimation, a direct comparison between two methods was rarely done in previous research. In this study, we aimed to explore a new methodology of processing LiDAR data in the context of a static measurement style, and compare ultrasonic sensor and LiDAR in terms of their plant height estimation performance.

3.2. Materials and Methods

3.2.1. Experiment Arrangement

The experiment was conducted in 2018 growing season at Agronomy Research Farm in Lincoln, NE, USA (40.86027°N, 96.61502°W). The experimental field contained 100 wheat plots where an augmented design with 10 checks replicated twice was used. The wheat lines consisted of 80 wheat genotypes produced at University of Nebraska–Lincoln, NE, USA. The planting was done at October 20th, 2017, and the plots were harvested at June 29th, 2018.

Five data collection campaigns occurred over the season. Each time the 100 plots were scanned by the ground phenotyping system (Figure 3.1). The plots were also measured by a yardstick using two methods depending on the growth stage (Table 3.1). At vegetative stages plant height was measured from soil surface to the top of stem, or apical bud (method A). At reproductive stages plant height was measured from soil

surface to the top of spike excluding awns (method B). For each plot three measurements were taken and averaged as the reference height of the plot.

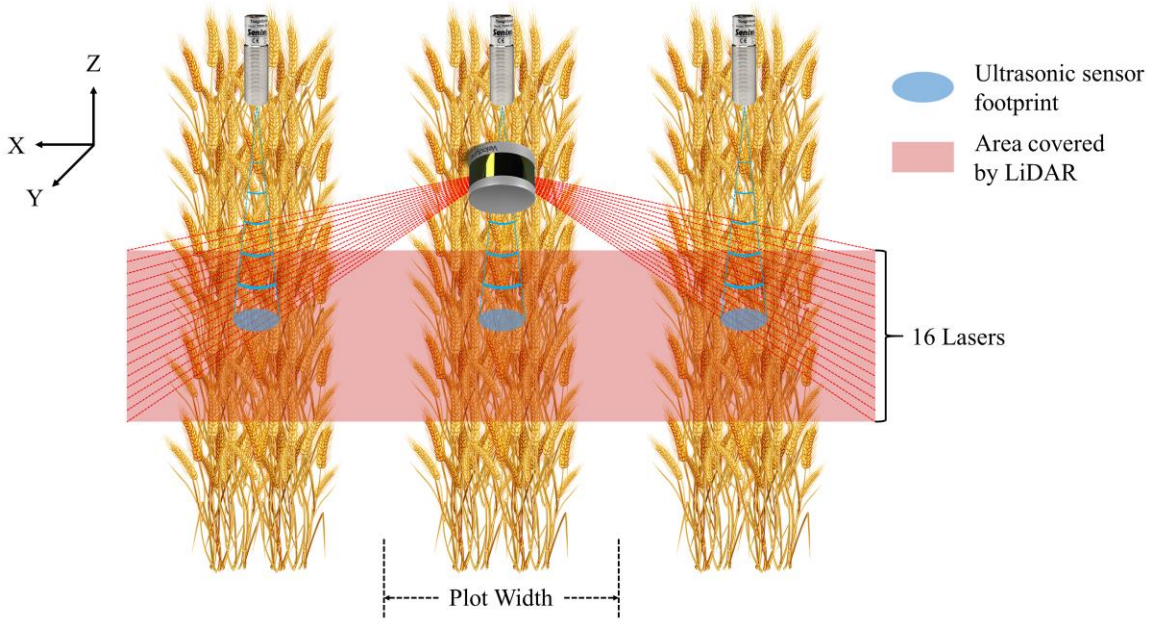

Figure 3.1. Schematic diagram showing the scanning areas of LiDAR and ultrasonic sensors at each measurement.

Table 3.1. Data collection campaign dates of manual measurement and the ground system for wheat height evaluation.

Data Collection Campaign	Growth Stage	Manual		Ground System
		Date	Method	Date
1st	Jointing stage: Feekes 6	May 7th	A	May 7th
2nd	Flag leaf stage: Feekes 8	May 15th	A	May 15th
3rd	Boot stage: Feekes 9	May 23rd	B	May 23rd
4th	Grain filling period: Feekes 10.5.3	May 31st	B	May 31st
5th	Physiological maturity: Feekes 11	June 16th	B	June 15th

3.2.2. Sensor and Software Setup

The measurement rate of ultrasonic sensors was set at 20 Hz. Since only half of the full azimuth range could be possibly useful for our application of scanning crop canopies (Figure 3.1), the LiDAR's horizontal FOV range was configured as 180°, and a 0.1° horizontal resolution was adopted for higher precision. The sensor was also configured to report the strongest return for each laser firing.

Voltage signals from ultrasonic sensors were converted to distances in the program through an equation calibrated in lab:

$$D = 29.116V + 11.641, \tag{3.1}$$

where D is distance in meters and V is sensor signal in volts. Ultrasonic canopy heights were then calculated as:

$$H_c = H_s - D, \tag{3.2}$$

where H_c is ultrasonic canopy height and H_s is ultrasonic sensor height. *Hs* was determined by measuring the distance between the sensors and soil surface before data collection, and LiDAR height was determined in the same way.

The subVI developed for LiDAR was incorporated in the while loop of the main program. The subVI receives data packets from LiDAR through User Datagram Protocol (UDP). Each data packet contains azimuth and distance information of all 16 lasers, and the subVI extracts and converts the information into a 3D Cartesian coordinate system. The origin of the coordinate system is defined as shown in Figure 3.2. After acquiring the XYZ coordinates of the points, the subprogram trims the point cloud in X dimension using a threshold of ±1.5×"plot width" (Figure 3.1) to delete points outside the desired

range. “Plot width” is defined as the distance between the middles of two adjacent alleyways, which was 1.524 m in this study. Figure 3.3 is an example of a raw point cloud captured by LiDAR.

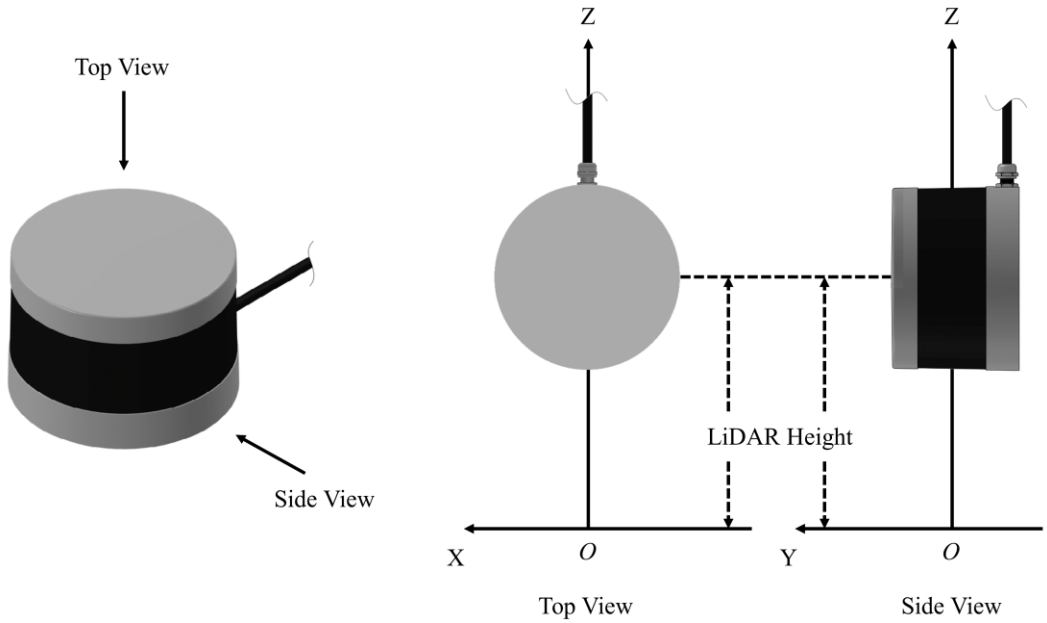

Figure 3.2. The Cartesian coordinate system for LiDAR point cloud at each measurement.

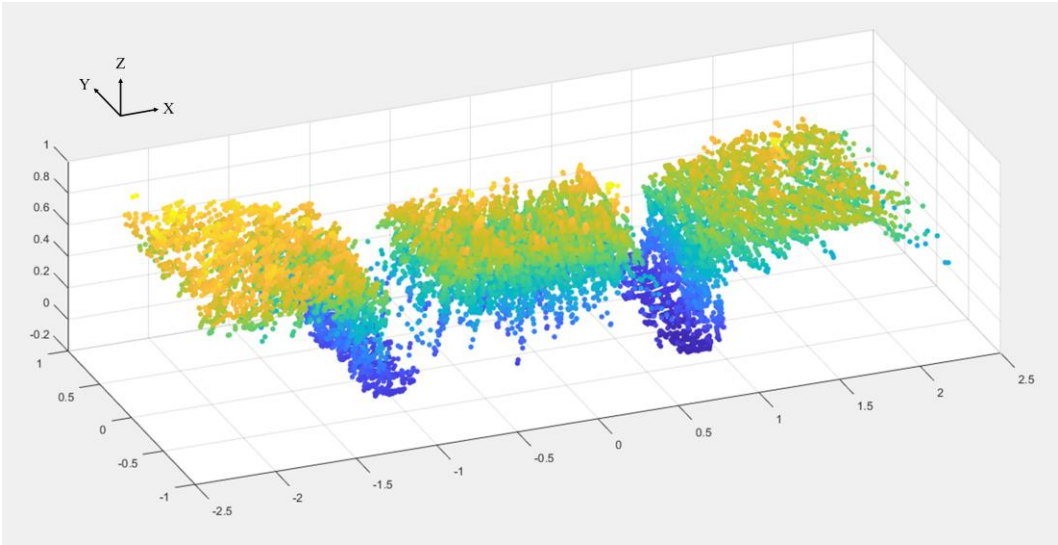

Figure 3.3. An example of raw LiDAR point cloud at each measurement.

3.2.3. Height Extraction from LiDAR Point Clouds

One issue that we encountered often in the field was the slant of the phenocart along with the sensor bars due to the unevenness and slope of ground (Figure 3.4). Corresponding LiDAR point clouds thus would show the tilted angle in the Cartesian coordinate system. In order to obtain accurate canopy height estimations from LiDAR, a pre-processing was performed for all raw point clouds to correct for this slanting issue before extracting height information. One assumption for the pre-processing is that the ground slope variation between the three plots within LiDAR's horizontal FOV can be ignored. LiDAR point clouds were processed using MATLAB R2017a (The MathWorks, Inc., Natick, MA, USA).

Figure 3.4. The slanting issue of the phenocart in field.

It is reasonable to speculate that the points of a point cloud without the slanting issue should be evenly distributed along the Y dimension considering plants with the

same genotype should have similar heights. A linear least-squares curve was fitted to the Y-Z plane (Figure 3.5b). The slope of the fitted curve was then converted to an angle θ in radiance through the relationship:

$$\theta = arctan\ (slope). \tag{3.3}$$

The point cloud was finally rotated clockwise by the angle θ (Figure 3.5c). The rotation center could be set at any point, as later the point cloud will be repositioned in the Z dimension.

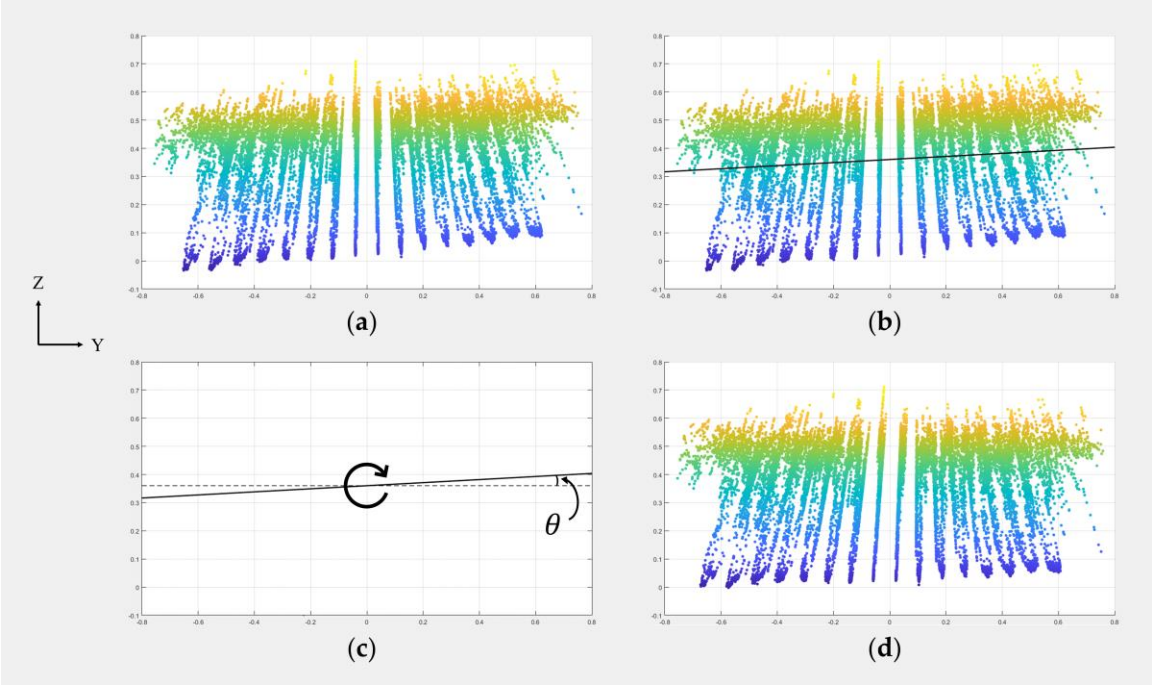

Figure 3.5. An example of Y-Z plane rotation correction: (a) Point cloud before rotation; (b) Fit a linear curve to points on Y-Z plane; (c) Rotate points on Y-Z plane by the angle θ; (d) Point cloud after rotation.

A similar procedure was also undertaken for the X-Y plane, which could be skipped as the slanting issue of point clouds on X-Y plane was minimum.

As the point distribution along the X-dimension could not be assumed to be even because points were representing plants with different genotypes, linear curve fitting couldn't be directly applied to the X-Z plane. The method proposed here was to find the rotation angle by finding the average Z value difference between the ground points of two alleyways.

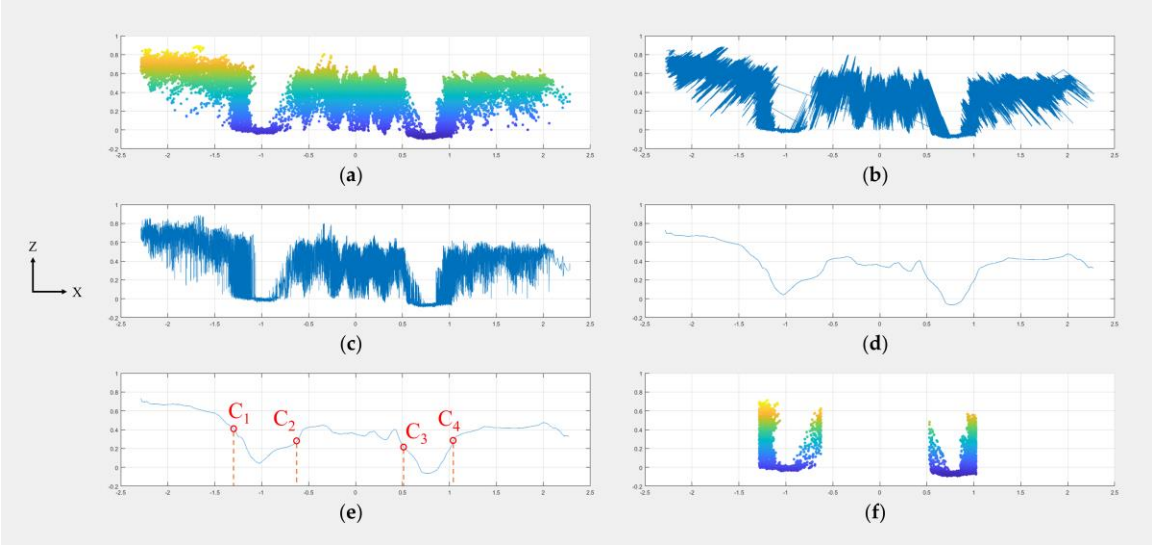

Figure 3.6. An example of extracting coarse alleyway point clouds: (a) point cloud before rotation; (b) line graph before sorting; (c) line graph after sorting; (d) smoothed line; (e) positions of the four most significant changes; (f) deletion of points beyond the desired range.

The points were first sorted by their X values so that the line graph of the points on the X-Z plane would have a horizontal curve (Figure 3.6c). Then, a moving average filter with a 0.05-m span was applied to smooth the curve (Figure 3.6d). Since the FOV of LiDAR could cover two alleyways, the trend of the curve typically had four abrupt changes in the Z dimension as lasers would scan from the canopy to the ground and back

to the canopy twice. After finding the position of the four most significant changes (Figure 3.6e), points with X values smaller than C_1, larger than C_4, or between C_2 and C_3 were deleted so that the portion of point cloud that contained two alleyways in the X dimension was extracted (Figure 3.6f).

The point cloud containing two alleyways (Figure 3.6f) was separated into left and right alleyway point clouds using the border of X=0. The non-ground points of two alleyway point clouds were further removed using the procedure explained below.

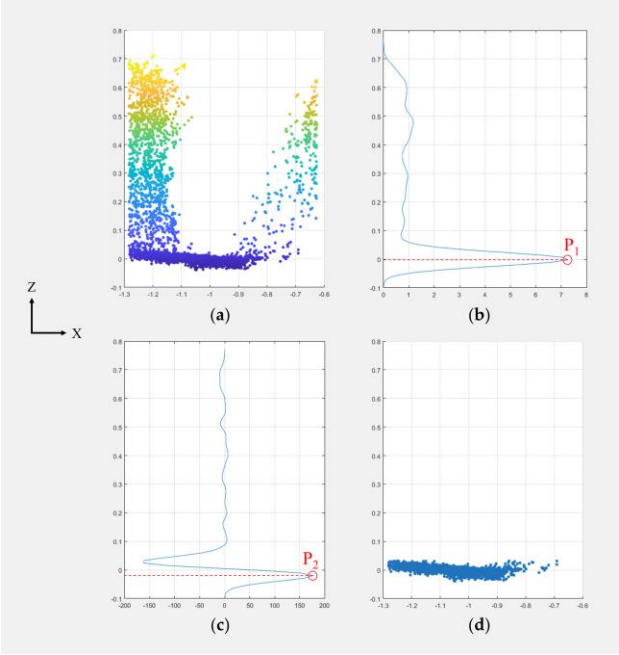

Figure 3.7. An example of extracting a refined alleyway point cloud: (a) point cloud of ground before cleaning; (b) point cloud kernel density in the Z dimension; (c) first derivative of the kernel density; (d) point cloud of ground after cleaning.

The kernel density in terms of Z values of the alleyway point cloud was first estimated (Figure 3.7b). As the points of ground were typically clustered at the bottom of

the Z axis, a dominant peak P_1 could be observed from the kernel density graph, which was also the first peak in the Z axis direction. The first derivative of the kernel density curve was calculated (Figure 3.7c). Assuming ground points follow a normal distribution in the Z dimension, the first peak P_2 of the first derivate curve in the Z axis direction would be the inflection point of the normal distribution, and the distance between P_1 and P_2 would be one standard deviation of the distribution. For a normal distribution, the range $\mu \pm 2\sigma$ includes about 95.45% of the values. Here a threshold of $\mu+2\sigma$ on the Z axis was used to separate non-ground points from ground points, where μ is P_1 and σ is P_1-P_2, and points with Z values larger than the threshold were deleted (Figure 3.7d).

After combining refined left and right alleyway point clouds (Figure 3.8a), a linear least-squares curve was fitted to the combined alleyway point cloud on the X-Z plane (Figure 3.8b), and the point cloud with the Y-Z and X-Y plane rotation correction performed (Figure 3.6a) was rotated by the angle φ, which was derived from the slope of the fitted curve (Figure 3.8c).

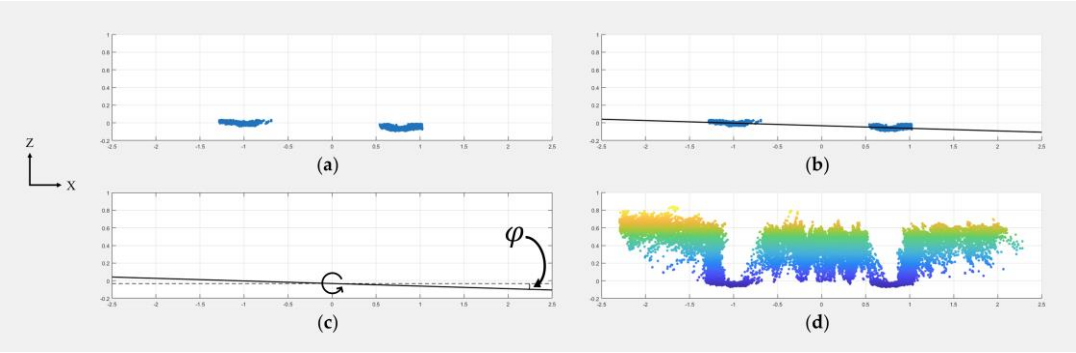

Figure 3.8. An example of X-Z plane rotation correction: (a) point cloud of ground before rotation; (b) linear curve fitted to ground points on the X-Z plane; (c) rotation of points on the X-Z plane by the angle φ; (d) point cloud after rotation.

The logic of the X-Z plane rotation correction was again executed on the point cloud with the X-Z plane rotation correction already performed (Figure 3.8d) to extract the rotated and refined alleyway point clouds (Figure 3.9a). The average Z value of the alleyway point cloud was calculated (Figure 3.9b), and the Z values of the whole point cloud (Figure 3.9d) were adjusted so that the average Z value of the alleyway point cloud would be located at 0.

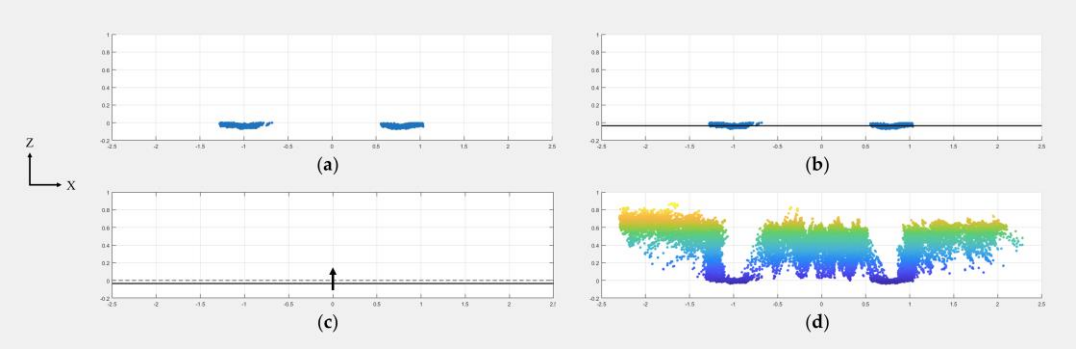

Figure 3.9. An example of ground baseline correction: (a) point cloud of ground before shifting; (b) the mean in the Z dimension; (c) points on the X-Z plane shifted by the offset; (d) point cloud after shifting.

The mean X values S_1 and S_2 of two alleyway point clouds were calculated (Figure 3.10b) and used as the border between different plots to split the point cloud (Figure 3.10c). Cumulative Z value percentiles of a point cloud with 0.5 percentage interval from 0 to 100 percent were extracted from each of the three split point clouds. In total there were 200 height values extracted and investigated for each plot.

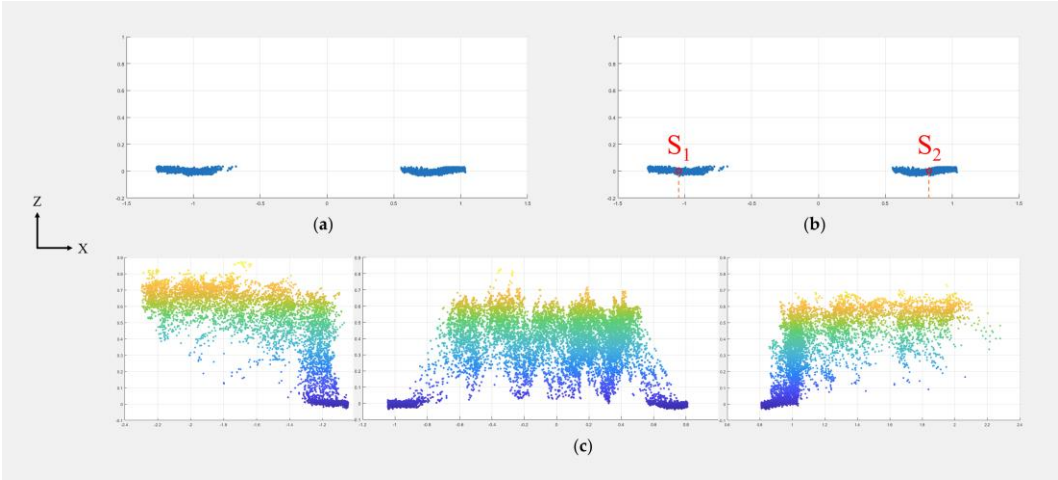

Figure 3.10. An example of splitting a point cloud: (a) point cloud of ground after rotation and shifting; (b) the mean in the X dimension for each side; (c) point cloud of each plot after splitting.

3.3. Results

3.3.1. Raw Point Clouds versus Processed Point Clouds

To evaluate the effectiveness of LiDAR point cloud pre-processing, plant heights were also extracted from all raw point clouds. With manual measurements being the standard, the minimum RMSE and the corresponding percentile of raw point clouds and processed point clouds at each data collection campaign were compared (Table 3.2).

The point cloud pre-processing consistently improved the precision of LiDAR's plant height estimation by lowering the minimum RMSE at different data collection campaigns by 12.85 to 44.95%, which confirmed its effectiveness of reducing the influence from uneven ground surface on point clouds.

Table 3.2. Optimal RMSE and percentile of raw and processed point clouds at each data collection campaign.

Data Collection Campaign		1st	2nd	3rd	4th	5th
Raw Point Clouds	Minimum RMSE (m)	0.0462	0.0389	0.0643	0.0467	0.0521
	Optimal Percentile	67.5th	85th	99.5th	99th	99.5th
Processed Point Clouds	Minimum RMSE (m)	0.0290	0.0300	0.0354	0.0407	0.0420
	Optimal Percentile	60th	91st	99th	99th	99.5th

3.3.2. LiDAR Height Estimation Performance by Date, Manual Method and Plot Position

By comparing to manual measurements, RMSE, Bias and R^2 of the heights extracted at each of the 200 percentiles of the processed point clouds across five data collection campaigns were investigated (Figure 3.11).

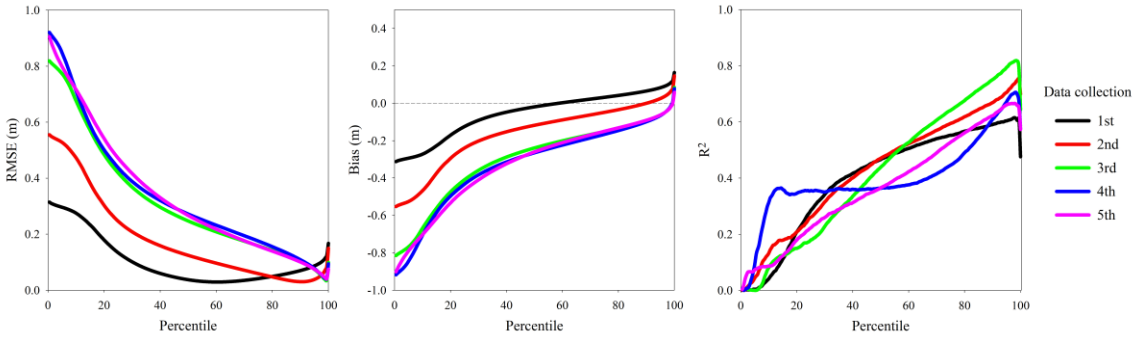

Figure 3.11. RMSE, Bias and R^2 of heights extracted at different percentiles from processed LiDAR point clouds over five data collection campaigns.

For a point cloud, low percentiles of Z value represent the height of ground, and high percentiles represent the height of vegetation above ground. Since the height of a wheat plot was never measured as the height of the tallest plant, it is easy to understand why RMSE dropped as percentile increased and raised again when percentile approached

100 percent. At the percentiles of the minimum RMSE, the average Bias over five data collections was -0.0011 m, which demonstrated LiDAR's accuracy. The percentiles for maximum R^2 fluctuated in between 98 and 99 percent, which did not seem to agree with the percentiles of minimum RMSE for the first two data collection campaigns (Table 3.2).

Considering the percentile of minimum RMSE could always vary if data were collected at different dates, the optimal percentile at each individual data collection campaign was impractical. Instead of treating all data collection campaigns equally and chose one universal percentile, we classified the 1st and 2nd data collection campaigns as method A category, and the 3rd, 4th and 5th data collection campaigns as method B category (Table 3.1) for more precise height estimations. RMSE of method A category, method B category and all category meaning treating all five data collection campaigns as a whole were compared (Table 3.3).

Table 3.3. Effects of manual method and plot position on minimum RMSE of processed LiDAR point clouds.

Category	Method A		Method B		All	
Number of Plots	200		300		500	
Minimum RMSE (m)	0.0478		0.0398		0.0657	
Optimal Percentile	82nd		99th		98th	
Sub-category	Side	Middle	Side	Middle	Side	Middle
Number of Plots	140	60	200	100	340	160
Minimum RMSE (m)	0.0436	0.0491	0.0395	0.0327	0.0649	0.0624
Optimal Percentile	77th	89th	99th	99.5th	97th	99th

Meanwhile, the effect of plot position on RMSE was investigated as well (Table 3.3). LiDAR had a fixed horizontal resolution, due to which the closer one object was to LiDAR the denser point cloud of that object would be acquired. In our case, the point cloud generated at each measurement included two side plots and one middle plot, and LiDAR was positioned above the middle plot, thus middle plots had denser point clouds than side plots. On average the point clouds of side plots had about 6000 points while the ones of middle plots had about 8000 points.

Based on Table 3.3, manual method affected RMSE substantially as the minimum RMSE of all category was 37.45% and 65.08% higher than the minimum RMSE of method A and B categories respectively, thus it makes more sense to use different optimal percentiles for two method categories for future work. However plot position didn't seem to affect RMSE in a significant way, with an average RMSE increase of 0.0026 m when plot positions weren't differentiated in two method categories, hence the effect of plot position can be ignored in the future as the additional RMSE should be minor.

3.3.3. Height Estimation Comparison between Ultrasonic Sensor and LiDAR

Over five data collection campaigns, ultrasonic senor estimated canopy heights and LiDAR estimated canopy heights where 82^{nd} and 99^{th} Z value percentiles of processed point clouds were chosen for method A and B categories were plotted against manual measurements (Figure 3.12).

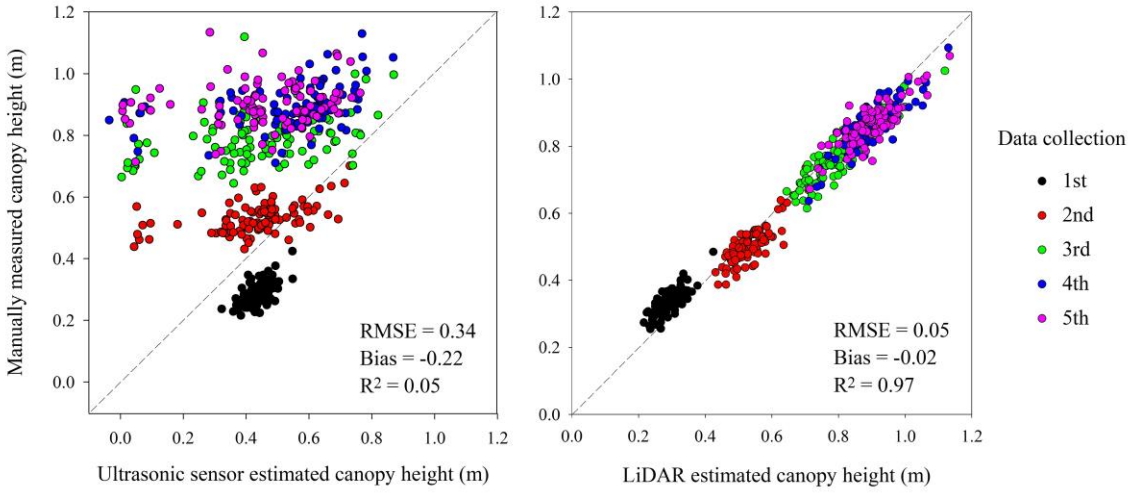

Figure 3.12. Ultrasonic sensor and LiDAR estimated canopy heights versus manually measured canopy heights.

Among two methods, LiDAR performed much better than ultrasonic sensors. With a large RMSE of 0.34 m and a low R^2 of 0.05, ultrasonic sensors tended to overestimate wheat canopy heights at the 1st data collection campaign and underestimate heights at the rest data collection campaigns, also it provided some negative readings, which will be discussed in Section 3.4.1. LiDAR provided precise and accurate height estimations throughout the season, with a low RMSE of 0.05 m, a low Bias of -0.02 m and a high R^2 of 0.97. In terms of the results, LiDAR can be considered as a reliable plant height evaluation method.

3.4. Discussion

3.4.1. Ultrasonic Sensor

The poor performance of ultrasonic sensors in this study can be explained by sensor limitations, wheat morphology and our measurement style. Ultrasonic sensor

generates sound waves to detect distances. When the sound waves are not reflected straight back to the sensor, due to either sensor orientation or object surface orientation, ultrasonic sensor may not capture the reflected sound waves. In this study the slanting issue of the phenocart could be a cause for that. Also when the surface of an object is not large enough to create strong echoes, ultrasonic sensor may not treat the weak echoes as valid signals. A typical wheat plant has narrow leaves and thin spikes, thus making it hard for ultrasonic sensors to pick up valid signals reflected from wheat. Moreover, because of our static measurement style, for each plot the ultrasonic sensor was only able to sample a small area (about 0.05 m^2 assuming one meter distance between sensor and canopy) to represent the whole plot. Due to within-plot variation, the random error from sampling could not be assessed or corrected, which led to ultrasonic sensors' low performance. Andújar et al. (2012) also used ultrasonic sensors in a static measurement style to detect weeds in wheat plants, and a low Pearson's correlation of 0.32 between ultrasonic sensor readings and manually measured wheat heights was observed.

The overestimation and underestimation of wheat height by ultrasonic sensors are illustrated in Figure 3.13. For a young wheat plant, clustered leaves with natural curvature seemed to reflect sound waves effectively, however the reference height was measured as the height of stem top instead of leaf top (method A). As wheat plants grew taller and started to emerge spikes, only the vegetation at the bottom seemed to have sufficient density to reflect strong echoes, which was lower than the manually measured spike tip height (method B).

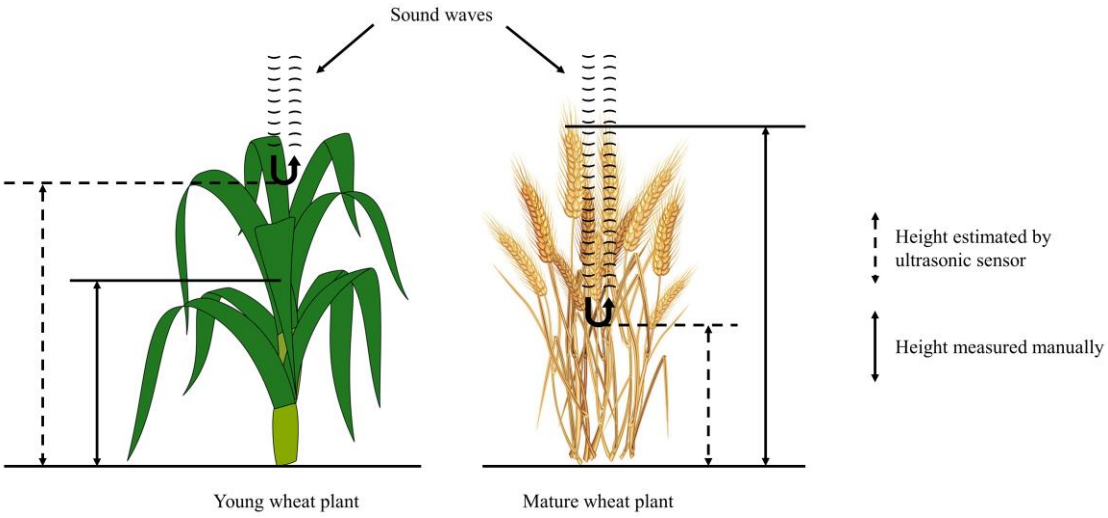

Figure 3.13. Two scenarios where ultrasonic sensor estimations disagree with manual measurements.

Near-zero canopy heights can appear when ultrasonic sensors cannot detect any significant echoes except for those reflected from ground. Moreover, if the phenocart is slanted so that the distance between ultrasonic sensors and ground at a given moment is larger than H_s in Equation 3.2, negative canopy heights will be recorded.

To improve plant height estimation of ultrasonic sensors, a continuous measurement style—i.e., multiple measurements per plot—is preferred. In a previous study by Scotford and Miller (2004), approximately 180 wheat height measurements from ultrasonic sensor were recorded for each plot, and it was found that the 90% percentile of each data set provided the best wheat height estimation, with the lowest RMSE for a wheat variety of 0.046 m. Pittman et al. (2015) extracted 25 to 30 ultrasonic sensor readings per wheat plot, and found a Pearson's R of 0.85 compared to manual measurements.

The continuous measurement style is superior to static measurement in terms of

obtaining better ultrasonic height estimations. In the context of our manned multi-sensor system, however, the phenocart was often required to stop to capture images. Two issues could occur if a continuous measurement style were adopted for the system: first, due to the highly variable phenocart speed on a field with a rough surface, inconsistent numbers of height measurements could be recorded for different plots; second, a large number of repeated measurements will be taken from the same sampling area when the phenocart is stationary. Both issues can Bias the data and make them troublesome to process. The static measurement style may, therefore, still be preferable for our system, in which case the ultrasonic sensor is not the best method for wheat height estimation.

3.4.2. LiDAR

The LiDAR point cloud pre-processing proposed in this study effectively reduced the influence from the slanting issue of the phenocart on the field. However, when ground is fully covered by vegetation, LiDAR with strongest return mode might not capture enough ground points, and pre-processing of the point cloud could not be undertaken. Due to the beam divergence of the lasers, a single firing of a laser can hit multiple objects resulting in multiple returns, and, typically, LiDAR can be configured to report multiple returns. A suggested solution is to configure LiDAR in multiple return mode since the last return signal has a higher chance of being reflected by soil, so a sufficient amount of ground points might be collected.

For processed point clouds, the minimum RMSE and the corresponding percentile increased as wheat grew taller (Table 3.2). As method B was measuring the tip of wheat spikes while method A was measuring the top of wheat stems, it was expected that the

optimal percentiles increased with data collection campaigns. Wind was suspected to be the reason for the increasing RMSE. As wheat plants get taller, wind can cause a larger degree of bending in plants, and LiDAR can capture deformed point clouds due to wind. At the fifth data collection campaign, when the minimum RMSE was the largest, the wind speed on the field was maintained at 8.0 to 8.9 m/s, with gust speeds up to 14.8 m/s.

Generally, extracting plant heights from point clouds can include the following steps: soil level estimation, noisy point removal, rasterization of the point cloud, and percentile selection. Similar to the purpose of our ground baseline correction (Yuan et al. 2018), most studies removed the effect of uneven soil levels by subtracting the corresponding soil height from vegetation points. The peak of a point cloud's Z value histogram (Jimenez-Berni et al. 2018; Madec et al. 2017), mean height of non-vegetation points (Deery et al. 2014), vehicle wheel contact points (Underwood et al. 2017) and direct soil measurement at the beginning of the season (Friedli et al. 2016) have all been used to estimate soil level. Some studies have also assumed constant distance between sensor and ground (Sun et al. 2017). LiDAR can detect spurious points in very bright light conditions (Jimenez-Berni et al. 2018), and some studies (Jimenez-Berni et al. 2018; Madec et al. 2017) removed outlier points by the method proposed by Rusu et al. (2008). We did not perform any noise removal technique, since even if a small number of erroneous points existed, they would not affect our optimal percentile significantly. Point clouds are sometimes rasterized for easier future data analysis, and statistics such as maximum, mean and certain percentiles are calculated for each grid or pixel. We preferred point clouds over 2D height maps because rasterization can cause loss of

information. “Percentiles” of point clouds are essentially plant heights, and 95th (Deery et al. 2014), 95.5th (Jimenez-Berni et al. 2018), 99.5th (Madec et al. 2017) and 100th percentiles (Sun and Li 2016; Sun et al. 2017) have all been adopted in different studies.

Compared to the results of other relevant studies on wheat height estimation using LiDAR, such as R^2 of 0.90 and RMSE of 3.47 cm from Madec et al. (2017), R^2 of 0.88 and 0.95 at two different months from Underwood et al. (2017), R^2 of 0.993 and RMSE of 0.017 m from Jimenez-Berni et al. (2018), and R^2 of 0.86 and RMSE of 78.93 mm from Deery et al. (2014), this study demonstrated the practicality of obtaining adequate wheat canopy height estimations using LiDAR based only on a section of a plot instead of the whole plot. The advantage here was higher system throughput and easier data processing, but the downside might be lower precision for plant height estimation. In this study, the advantage of 3D LiDAR technology allowed us to adopt a static measurement style, whereas for a 2D LiDAR, the continuous motion of the sensor is a necessity for generating 3D point clouds.

To improve LiDAR’s plant height estimation performance, in the context of our static measurement style, denser point clouds—i.e., collecting more data packets—might provide more consistent results. In this study, due to the insufficient number of data collection campaigns, our data did not cover all the important growth stages, thus we were unable to categorize data collection campaigns by growth stage. For future work optimal percentiles at each growth stage of wheat can be further investigated and established, which should provide more precise and accurate plant height estimations.

3.5. Conclusions

In this study, our proposed LiDAR point cloud pre-processing was demonstrated to be effective at reducing the influence of an uneven ground surface, and a LiDAR point cloud generated from a section of a plot was proven to be sufficient for providing precise and accurate plant height estimates. This methodology can be a reference for future studies that wish to adopt a static measurement style. The ultrasonic sensor, when used for plant height estimation in a static measurement style, is not suggested for plants with tall sward structures, such as mature wheat plants. In conclusion, LiDAR is recommended as a reliable alternative method for wheat height evaluation.

CHAPTER 4

EARLY PREDICTION OF SOYBEAN TRAITS THROUGH COLOR AND TEXTURE FEATURES OF CANOPY RGB IMAGERY[2]

4.1. Background

Increasing population, growing meat and dairy consumption and rising biofuel usage are key factors for the climbing global demand for crop production (Ray et al. 2012, 2013). By 2050, a 60 to 110% increase in world's agricultural production may be needed to meet the projected demand (Ray et al. 2013; Tilman et al. 2011), which is known as the 2050 challenge. Ray et al. (2013) found that, globally, the average increase rates of yield from 1961 to 2008 for four major crops—maize, rice, wheat, and soybean, are far below the adequate level to meet future demands. Doubts even exist for our ability to maintain current crop yield in the context of a rapidly changing global environment (Tester and Langridge 2010). More land clearing for agriculture and improving the productivity of existing cropland are two solutions for the challenge (Tilman et al. 2011), however the later solution is preferred (Ray et al. 2013).

Crop productivity can be improved through crop breeding and advanced management practices. Crop breeding aims to improve crop genetic makeup for more desirable traits such as higher yield, however the improvement rate of modern crop breeding in terms of genetic gain is insufficient for the 2050 challenge (Li et al. 2018).

---

[2] This chapter is a portion of a submitted manuscript: Yuan, W., Wijewardane, N. K., Jerkins, S., Bai, G., Ge, Y., & Graef, G. L. (2019). Early Prediction of Soybean Traits through Color and Texture Features of Canopy RGB Imagery.

Partially, this slow improvement rate is due to the long crop generation cycles (Watson et al. 2018). Newly emerged methods such as “speed breeding”, which utilizes prolonged photoperiods, can increase the generation cycles of various crops in greenhouse from 2-3 to 4-6 per year (Watson et al. 2018). However, a greenhouse cannot fully mimic field conditions, plus it has limited space and a high running and maintenance cost. In order to select the crop genotypes that are suitable for extensive agricultural production, breeding in field is irreplaceable. Since field environment cannot be easily altered by humans, the concept of “speed breeding” cannot be realized in field in the same way as if in greenhouse, and alternative methods are needed for accelerating crop breeding research.

The phenotype of a plant results from the interaction between its genotype and environment, and it reflects plant performance under a certain environment. Since the genotype of a plant does not change throughout the course of growth, relationships might exist between the plant phenotypes at different time points. If plant traits at the end of a season such as yield can be predicted by plant phenotyping at early-season, breeders then do not have to wait for a full crop generation cycle to make genotype selections, thus the speed of crop breeding can be improved. Attempts for early prediction of plant traits have been made in previous research. For example, predicting soybean yield using NDVI measured at reproductive stages (Ma et al. 2001); predicting sugar and fiber content of sugarcane at maturity using the corresponding values measured months before the harvest (Elibox 2012); predicting leaf nitrogen concentration of almond in summer using leaf nitrogen and boron concentrations in spring (Saa et al. 2014); predicting grapevine yield using the number of berries detected at fruit development stages (Aquino et al. 2018).

To select a phenotyping method that is suitable for large-scale crop breeding research, it needs to be non-destructive and efficient. Advanced instruments such as light detection and ranging (LiDAR) or hyperspectral camera can provide rich information about a plant, however they are typically expensive and can be difficult for people with agronomy background to use. Red-green-blue (RGB) cameras, on the other hand, have been widely and long employed in agricultural research. They are cheap and user-friendly, and modern models are able to capture images in very high spatial resolutions. With the popularization of smartphones, RGB cameras also have high accessibility. Many well-developed image processing and analysis techniques allow various features from RGB images to be extracted and analyzed, however few have been studied for crop trait early prediction purpose.

Color and texture are two important aspects in digital imagery. Color is the characteristic perceived by human visual system. The color of a plant is closely related with plant physiology. In an image, the color feature of a plant can be used for, for example, plant segmentation (Hamuda, Glavin, and Jones 2016), plant stress assessment (Bai et al. 2018), disease spot detection (Chaudhary et al. 2012), or estimating plant traits such as ground cover (Ritchie et al. 2010), biomass (Hunt et al. 2005), leaf chlorophyll content (Hunt et al. 2011) and leaf nitrogen concentration (Wang et al. 2014). Many vegetation indices based on RGB bands have been developed and studied for accomplishing the tasks. Textures, though lacking a formal definition, are visual patterns consisted of entities with certain characteristic in terms of color, shape, size, etc. The properties of the entities give the perceived coarseness, smoothness, randomness, uniformity, etc., that are eventually regarded as texture (Materka and Strzelecki 1998).

The essence of texture in digital imagery is the spatial arrangement of pixels with various gray levels (Bharati, Liu, and MacGregor 2004). Texture analysis is important in many areas such as remote sensing and medical imaging, and its common applications include image segmentation, image classification, and pattern recognition (Bharati et al. 2004). Although various texture analysis techniques exist, texture features derived from gray-level co-occurrence matrix (GLCM) are the most popular because of their simplicity and adaptability (Zhang et al. 2017). Details regarding GLCM calculation would be reviewed in the next section. The color co-occurrence matrix (CCM) method was first reported by Shearer and Holmes in 1990 (Shearer and Holmes 1990), where GLCMs were computed from image color channels, instead of being calculated from grayscale images. Interestingly, CCM method has never been applied to vegetation index images such as NDVI images, and the value of texture information of such images has never been investigated to the author's knowledge.

The goal of this study was to explore the possibility of early prediction of soybean traits through canopy RGB imagery. More specifically, the objective is to identify which soybean traits might be predictable using color and texture features of early-season canopy RGB images. CCM method was used for extracting texture features, and nine soybean traits were selected as case-study traits. In addition to the original RGB images, theoretical and empirical transformations of RGB images, namely images in alternative color spaces and vegetation index images based on RGB bands were also computed for additional color and texture features.

4.2. Gray-Level Co-Occurrence Matrix Review

GLCM, originally called gray-tone spatial-dependence matrix, was first introduced by Haralick et al. in 1973 (Haralick, Shanmugam, and Dinstein 1973). It describes the joint probability of pixel pairs at any gray-levels, thus is able to represent the texture of an image statistically. GLCM-based texture features have many applications in agricultural research, and some examples were listed in Table 4.1.

Table 4.1. Examples of agriculture-related research utilizing GLCM-based texture features

Statistical Approach	Application	Case Study	Reference
Classification	Plant identification	Plant leaf identification using Flavia dataset (32 types of plants) and Foliage dataset (60 types of plants)	(Kadir 2014)
		Identification of grape, mango, chili, wheat, beans and sunflower affected by powdery mildew disease	(Pujari, Yakkundimath, and Byadgi 2014)
		Identification of five *Ficus deltoidea* varieties	(Nasir et al. 2014)
		Recognition of 31 classes of plant leaves	(Chaki, Parekh, and Bhattacharya 2015)
	Flower identification	Classification of 18 types of flower	(Siraj, Ekhsan, and Zulkifli 2014)
	Seed identification	Classification for individual kernels of wheat, barley, oats, and rye	(Majumdar and Jayas 2000)
		Classification of wheat and barley kernels	(Guevara-Hernandez and Gomez-Gil 2011)

		Identify four geographical origins of *Jatropha curcas* L. seeds	(Gao et al. 2013)
		Detection of freefalling wheat kernel damage	(Delwiche, Yang, and Graybosch 2013)
	Pollen identification	Identify ten types of pollen grains in honey	(Kaya et al. 2013)
	Disease identification	Classify lesions of three Phalaenopsis seedling diseases and uninfected leaves	(Huang 2007)
		Classify diseased wheat leaves at five severity stages	(Majumdar et al. 2015)
		Classify healthy, early blight and late blight diseased tomato leaves	(Xie et al. 2015)
		Classify early blight diseased eggplant leaves and heathy leaves	(Xie and He 2016)
		Identify two types of diseased grapevine leaves	(AlSaddik et al. 2018)
	Stress detection	Detection of three levels of drought stress in maize	(Jiang et al. 2018)
	Weed detection	Identify wild blueberry, weeds and bare spots in field	(Chang et al. 2012)
		Detection of weeds in rice fields	(Barrero et al. 2016)
		Classify vegetable and weed in filed	(Pulido, Solaque, and Velasco 2017)
	Plant mapping	Classification for corn, wheat, soya, pasture, and alfalfa using multipolarization radar data	(Anys and He 1995)
		Map invasive *Leucaena leucocephala* using QuickBird satellite imagery	(Tsai and Chou 2006)
		Map invasive *Fallopia japonica* using orthophotos	(Dorigo et al. 2012)
	Growth stage identification	Phenological stage classification of wheat, barely, lentil, cotton, pepper and corn	(Yalcin 2015)

Regression	Trait estimation	Improve the empirical relationship between leaf area index and normalized difference vegetation index of forest	(Wulder et al. 1998)
		Estimate age, top height, circumference, stand density and basal area of forest	(Kayitakire, Hamel, and Defourny 2006)
		Predict textural class, moisture content, leaf area index and leaf water potential of moss	(Ushada, Murase, and Fukuda 2007)
		Estimate forest biomass	(Sarker and Nichol 2011)
		Predict glucose, fructose, sucrose and total sugar content of muskmelon	(Wei et al. 2012)
		Predict moisture content of quince fruits being dried	(Bakhshipour, Jafari, and Babellahi 2013)
		Predict maize leaf moisture content	(Han et al. 2014)
		Estimate leaf nitrogen content of winter wheat	(Leemans et al. 2017)
		Count ear number of wheat growing in filed	(Zhou et al. 2018)

A GLCM can be mathematically expressed as $P(i,j,d,\theta)$, where i and j stand for the pixel intensity, or gray-levels of two pixels in a pixel pair, d stands for pixel displacement, and θ stands for scanning direction. Since calculating a GLCM over the full dynamic range of an image can be prohibitive, quantization is a common practice for reducing the number of gray levels of an image. For 8-bit images, which have 256 gray levels, quantization level can be 8, 16 or 32 (Clausi 2002). However, the tradeoff of this accelerated GLCM calculation is a reduction in image information.

Assume a 4×4 image with gray-levels specified, then the corresponding GLCM represents the numbers of pixel pairs in an image (Figure 4.1).

2	2	3	4
4	3	4	2
3	4	3	4
3	2	3	2

Image

$i \setminus j$	2	3	4
2	#(2,2)	#(2,3)	#(2,4)
3	#(3,2)	#(3,3)	#(3,4)
4	#(4,2)	#(4,3)	#(4,4)

Corresponding GLCM layout

Figure 4.1. Schematic diagram showing the GLCM layout of an image.

To calculate a GLCM, one needs to specify d and θ. d defines the distance between two pixels that can be considered as "a pair", which is typically set as 1, meaning two adjacent pixels are considered as a pair. θ defines the direction along which the pixel pairs lie. 0°, 45°, 90° and 135° are common scanning directions (Figure 4.2).

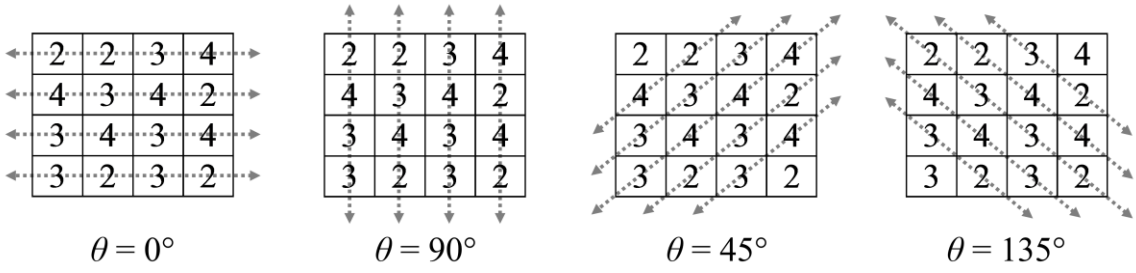

Figure 4.2. Common scanning directions for generating a GLCM.

The distinction between two opposite scanning directions is typically ignored, such as left to right versus right to left, since the resulting GLCMs are simply the transpose of each other, then symmetric GLCMs are employed as shown in Figure 4.3 (Conners and Harlow 1980), where both opposite directions are considered.

2	4	1
4	0	6
1	6	0

$P(i,j,1,0°)$

0	1	5
1	4	4
5	4	2

$P(i,j,1,90°)$

0	2	1
2	4	2
1	2	4

$P(i,j,1,45°)$

0	4	1
4	2	1
1	1	4

$P(i,j,1,135°)$

Figure 4.3. Symmetric GLCM examples of the sample image.

Before extracting texture features, GLCMs need to be normalized. $p(i,j,d,\theta)$ denotes the normalized GLCM, where:

$$p(i,j,d,\theta) = \frac{P(i,j,d,\theta)}{\sum_{i,j} P(i,j,d,\theta)} \tag{4.1}$$

as shown in Figure 4.4.

0.083333	0.166667	0.041667
0.166667	0	0.25
0.041667	0.25	0

$p(i,j,1,0°)$

0	0.038462	0.192308
0.038462	0.153846	0.153846
0.192308	0.153846	0.076923

$p(i,j,1,90°)$

0	0.111111	0.055556
0.111111	0.222222	0.111111
0.055556	0.111111	0.222222

$p(i,j,1,45°)$

0	0.222222	0.055556
0.222222	0.111111	0.055556
0.055556	0.055556	0.222222

$p(i,j,1,135°)$

Figure 4.4. Normalized GLCM examples of the sample image.

Texture features extracted from different GLCMs of the same image can be either averaged or treated as independent variables, though Haralick et al. suggested to use the averages (Haralick et al. 1973).

4.3. Materials and Methods

4.3.1. Data Collection

Soybean canopy images were collected in 2016 over plots distributed among four locations at V4/V5 growth stage using a multi-sensor phenotyping system (Bai et al. 2016), which was equipped with C920-C Webcams (Logitech, Lausanne, Switzerland).

Soybean plots belonged to 35 yield evaluation experiments in soybean breeding programs, within which the soybean populations were developed for different purposes, such as improved yield, improved genotype diversity, improved response to water, and improved seed quality metrics. In total 6383 images were captured over 5667 unique plots with measurements repeated for some plots. Among all plots, 2551 unique genotypes existed. Relevant information regarding the soybean plots and data collection were listed in Table 4.2. Images were stored as 8-bit png files with a 2304×1536 resolution.

Table 4.2. Soybean plot and data collection details.

Location	Date Planted	Date Harvested	Date Measured	Number of Images
Clay Center, NE	5/20/2016	10/20/2016	6/21/2016	1254
Cotesfield, NE	5/21/2016	10/2/2016	6/23&24/2016	1332
Mead, NE	6/3/2016	10/16/2016	7/6&8/2016	2555
Wymore, NE	6/4/2016	10/31/2016	7/10/2016	1242

4.3.2. Ground Truths

Nine soybean traits were selected for this study, which were defined as the following:

• Yield: seed volume in bushels per acre, adjusted to 13% moisture content, after the seeds have been dried to a uniform moisture content.

• Maturity: the number of days in between the planting date and the date when 95% of the pods have ripened. Delayed leaf drop and green stems are not considered in assigning maturity.

• Height: the average length from the ground to the tip of the main stem at maturity, measured in inches.

• Seed Size: seed weight in grams per 100 seeds.

• Protein, Oil, and Fiber: The protein, oil, and fiber concentration of a 70 g seed sample determined by an lnfratec 1229 whole-seed grain analyzer. All measurements are adjusted to a 13% moisture basis.

• Lodging: rated at maturity according to the following scores:

  ◦ 1: Most plants erect.

  ◦ 2: All plants leaning slightly or a few plants down.

  ◦ 3: All plants leaning moderately, or 25 to 50% down.

  ◦ 4: All plants leaning considerably, or 50 to 80% down.

  ◦ 5: Most plants down.

• Seed Quality: rated according to the following scores considering the amount and degree of wrinkling, defective seed coat (growth cracks), greenish ness, and moldy or other pigment:

  ◦ 1: Very good.

  ◦ 2: Good.

  ◦ 3: Fair.

  ◦ 4: Poor.

◦ 5: Very poor.

Not all ground truths were available for every plot measured. Table 4.3 shows the availability of different ground truths.

Table 4.3. The number of images having the corresponding ground truth available.

Ground Truth	Number of Images
Yield	6001
Maturity	4719
Height	3118
Seed Size	2372
Protein	2801
Oil	2801
Fiber	2801
Lodging	4719
Seed Quality	1866

4.3.3. Image Processing

4.3.3.1. Pre-processing

For the purpose of enhancing contrast and improving color consistency across images, the contrast of raw images were stretched by saturating the bottom 1% and the top 1% of all pixel values in R, G and B channels respectively. Assume a grayscale image $I(x,y)$, where x stands for pixel row position, and y stands for pixel column position. In our case, x and y range from 1 to 1536 and 1 to 2304. Then the contrast-enhanced image $E(x,y)$ would be:

$$E(x,y)=\begin{cases} L_N, I(x,y) < L_O \\ \dfrac{(I(x,y)-L_O)(U_N-L_N)}{U_O-L_O}+L_N, L_O \ll I(x,y) \ll U_O, \\ U_N, I(x,y) > U_O \end{cases} \quad (4.2)$$

where L_O and U_O are the original lower and upper limits, which are the 1st and 99th percentile of all pixel values in $I(x,y)$, and L_N and U_N are the new limits, which are 0 and 255 for 8-bit images.

Next, soil background was removed since it contained irrelevant information. It was challenging to segment plants under different lighting and shadowing conditions using one regular thresholding technique. Here we proposed a new plant segmentation method utilizing multiple vegetation indices to maximize segmentation accuracy.

First three vegetation index images were calculated from each contrast-enhanced RGB image: excess green (ExG) (Woebbecke et al. 1995), modified excess green (MExG) and color index of vegetation extraction (CIVE), where:

$$ExG=\begin{cases} -1, R=G=B=0 \\ \dfrac{2G-R-B}{R+G+B}, else \end{cases}, \quad (4.3)$$

$$MExG = 1.262G - 0.884R - 0.311B, \quad (4.4)$$

$$CIVE = 0.441R - 0.811G + 0.385B + 18.78745. \quad (4.5)$$

Each of the three vegetation index images was then rescaled to the range of 0 to 1 respectively. The difference image between MExG and CIVE was computed to further enhance the intensity difference between plant pixels and background pixels, then a binary mask $M1(x,y)$ was generated using Otsu's thresholding technique (Otsu 1979). A 0.5 threshold was applied to ExG to generate another binary mask $M2(x,y)$. Two masks

were overlaid to create the final mask $M(x,y)$ where:

$$M(x,y) = \begin{cases} NA, M1(x,y) = M2(x,y) = 0 \\ 1, else \end{cases} \quad (4.6)$$

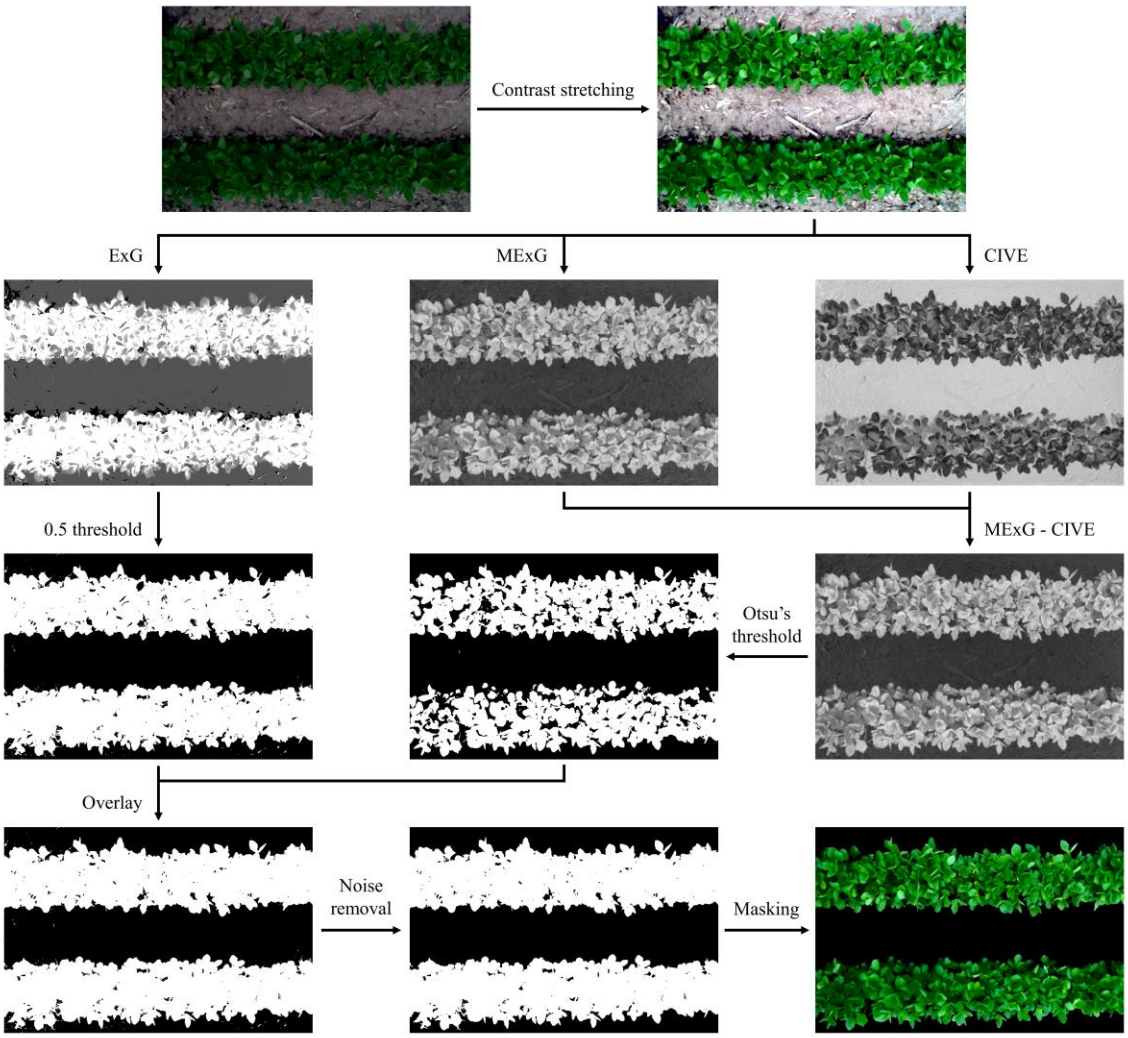

Figure 4.5. Flowchart of soybean canopy image pre-processing.

Instead of using 0, NA values were adopted here to avoid the influence of a large number of 0 in a masked image when computing color and texture features. The noise of $M(x,y)$ was cleaned by removing objects with 300 or fewer connected pixels. To this

point $M(x,y)$ was ready to be used for removing soil background from any images calculated later (Figure 4.5).

4.3.3.2. Image Transformations

Four common color spaces, and 20 vegetation indices based on RGB bands were selected to represent the theoretical and empirical transformations of RGB imagery (Table 4.4). Plus the original RGB color space, in total (1+4)×3+20=35 transformed images were calculated from each contrast-enhanced RGB image, then mask $M(x,y)$ was applied to all transformed images.

Table 4.4. List of theoretical and empirical RGB image transformations.

Type	Name	Abbreviation	Description	Note	Reference
Original	Red	R	R channel from RGB color space	Raw values were adjusted by contrast stretching. Values range from 0 to 255.	(Casadesús et al. 2007; Wang et al. 2014)
	Green	G	G channel from RGB color space		
	Blue	B	B channel from RGB color space		
Theoretical transformation	X	X	X channel from CIE 1931 XYZ color space	CIE 1931 2° Standard Observer; CIE Standard Illuminant D65	(Casadesús et al. 2007)
	Y	Y	Y channel from CIE 1931 XYZ color space		
	Z	Z	Z channel from CIE 1931 XYZ color space		
	L-star	L*	L* channel from CIE 1976 L*a*b* color space	CIE Standard Illuminant D65	(Wang et al. 2014)
	a-star	a*	a* channel from CIE 1976 L*a*b* color space		
	b-star	b*	b* channel from CIE 1976 L*a*b* color space		
	Hue	H	H channel from HSI color space		(Karcher and Richardson 2003; Wang et al. 2014)
	Saturation	S	S channel from HSI color space		
	Intensity	I	I channel from HSI color space		
	Y-prime	Y'	Y' channel from Y'CbCr color space		(Liu et al. 2018)
	Cb	Cb	Cb channel from Y'CbCr color space		
	Cr	Cr	Cr channel from Y'CbCr color space		
Empirical transformation	Normalized red	NR	$NR = \frac{R}{R+G+B}$	Equations simplified. Abbreviations also known as r, g, b.	(Woebbecke et al. 1995)
	Normalized green	NG	$NG = \frac{G}{R+G+B}$		
	Normalized blue	NB	$NB = \frac{B}{R+G+B}$		
	Excess red	ExR	$ExR = \frac{1.4R - G}{R+G+B}$	Equation simplified.	(Meyer, Hindman, and Laksmi 1999)
	Excess blue	ExB	$ExB = \frac{1.4B - G}{R+G+B}$	Equation simplified.	(Guijarro et al. 2011)

	Excess green red	ExGR	$ExGR = \frac{3G - 2.4R - B}{R + G + B}$	Equation simplified.	(Meyer and Neto 2008)
	Green blue difference	GBD	$GBD = G - B$		(Sanjerehei 2014)
	Red blue difference	RBD	$RBD = R - B$		
	Red green difference	RGD	$RGD = R - G$		
	Green red ratio	GRR	$GRR = \frac{G}{R}$		(Du and Noguchi 2017; Ritchie et al. 2010)
	Green blue ratio	GBR	$GBR = \frac{G}{B}$		(Sanjerehei 2014)
	Normalized green red difference	NGRD	$NGRD = \frac{G - R}{G + R}$	Also known as normalized difference index (NDI) or green red vegetation index (GRVI).	(Hamuda et al. 2016; Hunt et al. 2005)
	Normalized green blue difference	NGBD	$NGBD = \frac{G - B}{G + B}$		(Du and Noguchi 2017; Shimada et al. 2012)
	Modified normalized green red difference	MNGRD	$MNGRD = \frac{G^2 - R^2}{G^2 + R^2}$	Also known as modified green red vegetation index (MGRVI).	(Bendig et al. 2015)
	Visible band difference	VD	$VD = \frac{2G - B - R}{2G + B + R}$	Also known as green leaf index (GLI).	(Hunt et al. 2013; Louhaichi, Borman, and Johnson 2001)
	Red green blue vegetation index	RGBVI	$RGBVI = \frac{G^2 - B \times R}{G^2 + B \times R}$		(Bendig et al. 2015)
	Crust index	CI	$CI = \frac{2B}{R + B}$	Equation simplified.	(Sanjerehei 2014)
	Color index of vegetation extraction	CIVE	$CIVE = 0.441R - 0.811G + 0.385B + 18.78745$		(Kataoka et al. 2003)
	Triangular greenness index	TGI	$TGI = 95G - 35R - 60B$	Equation simplified.	(Hunt et al. 2011)
	Modified excess green	MExG	$MExG = 1.262G - 0.884R - 0.311B$		(Burgos-Artizzu et al. 2011)

For each of the 35 transformed images, if applicable, non-mask NA values and negative infinity values were replaced as the minimum real value of the image, and positive infinity values were replaced as the maximum real value of the image. All values of transformed images were stored in double format, meaning decimal places were not rounded. Figure 4.6 shows various texture patterns carried by different transformed images derived from the same RGB image. The images in Figure 4.6 were colorized for viewing convenience, and the color scheme corresponded to the value range of an image

before mask $M(x,y)$ was applied. Images were processed using MATLAB R2018b (The MathWorks, Inc., Natick, MA, USA).

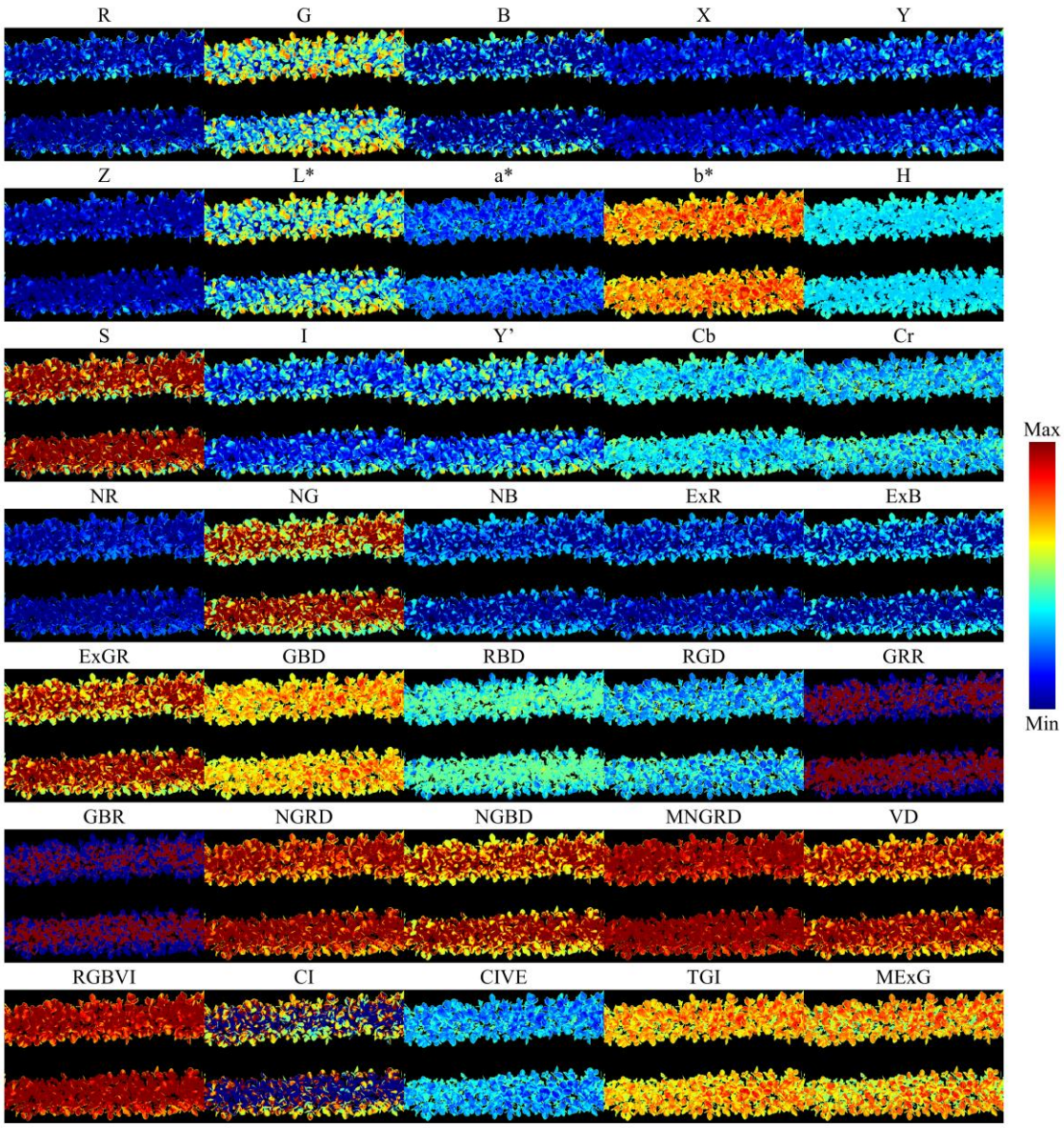

Figure 4.6. Examples of colorized transformed images containing different color and texture information.

4.3.4. Image Feature Extraction

4.3.4.1. Color Features

For each of the 35 transformed images, four color indices were calculated: mean (μ), standard deviation (σ), skewness (θ) and kurtosis (δ) (Kadir 2014). Since for each soybean plot the cameras were able to capture the majority of the canopy, we assume the plant pixels in each image follow a population distribution instead of a sample distribution.

Take a transformed image $T(x,y)$ where the number of plant pixels, or non-NA values is N, then:

$$\mu = \frac{\sum_x \sum_y T(x,y)}{N} \tag{4.7}$$

$$\sigma = \sqrt{\frac{\sum_x \sum_y (T(x,y) - \mu)^2}{N}} \tag{4.8}$$

$$\theta = \frac{\sum_x \sum_y (T(x,y) - \mu)^3}{N\sigma^3} \tag{4.9}$$

$$\delta = \frac{\sum_x \sum_y (T(x,y) - \mu)^4}{N\sigma^4} \tag{4.10}$$

Notice NA values from mask $M(x,y)$ were ignored in the calculations above. In total 35×4=140 color indices were derived from each original RGB image.

4.3.4.2. Texture Features

It is reasonable to assume that transformed images cannot contain more information than the original RGB image. Before extracting texture features, each of the

35 transformed images without mask $M(x,y)$ applied was first rescaled to 0 to 255 and rounded as integers to reduce computational complexity, then mask $M(x,y)$ was applied. Two symmetric GLCMs $p(i,j,1,0°)$ and $p(i,j,1,90°)$ were calculated from each transformed image. Notice NA values were ignored when computing GLCMs. Nine texture indices were calculated from each GLCM: maximum probability (MP), mean (MEA), variance (VAR), correlation (COR), angular second moment (ASM), entropy (ENT), dissimilarity (DIS), contrast (CON) and inverse difference moment (IDM) (Beliakov, James, and Troiano 2008; Haralick et al. 1973), where:

$$MP = max(p(i,j,d,\theta)) \tag{4.11}$$

$$MEA = \sum_{i,j} ip(i,j,d,\theta) = \sum_{i,j} jp(i,j,d,\theta) \tag{4.12}$$

$$VAR = \sum_{i,j} (i - MEA)^2 p(i,j,d,\theta) = \sum_{i,j} (j - MEA)^2 p(i,j,d,\theta) \tag{4.13}$$

$$\begin{aligned} COR &= \frac{\sum_{i,j}(i - MEA)(j - MEA)p(i,j,d,\theta)}{VAR} \\ &= \frac{\sum_{i,j} ijp(i,j,d,\theta) - MEA^2}{VAR} \end{aligned} \tag{4.14}$$

$$ASM = \sum_{i,j} p(i,j,d,\theta)^2 \tag{4.15}$$

$$ENT = -\sum_{i,j} p(i,j,d,\theta) log_2(p(i,j,d,\theta)) \tag{4.16}$$

$$DIS = \sum_{i,j} |i - j| p(i,j,d,\theta) \tag{4.17}$$

$$CON = \sum_{i,j} (i - j)^2 p(i,j,d,\theta) \tag{4.18}$$

$$IDM = \sum_{i,j} \frac{p(i,j,d,\theta)}{1+(i-j)^2} \quad (4.19)$$

After obtaining the same texture features from two GLCMs of the same image, such as MP of $p(i,j,1,0°)$ and MP of $p(i,j,1,90°)$, two texture indices were averaged as one. In total 35×9=315 texture indices were derived from each original RGB image.

4.3.5. Data Analysis

The dataset was randomly split into 70% and 30% segments for model calibration and validation. Regression technique Cubist was used to model for Yield, Maturity, Height, Seed Size, Protein, Oil and Fiber, and classification technique Random Forests was used to model for Lodging and Seed Quality. Since the RGB images were captured over different locations at different dates, we introduced another two variables to improve model robustness: Location and Time (LnT). Variable "Location" contained number 1, 2, 3 and 4 which represented four locations where the soybean plots grew. Variable "Time" was the number of days in between the planting date and the measuring date. All color and texture indices plus LnT (140+315+2=457 variables) were used as predictor variables. All predictor variables were standardized by removing the mean and scaling to unit variance before used for calibrating models. Model tuning was done through 10 random segment cross-validation. The data analysis was conducted in R language (R Core Team 2018) using package cubist (Kuhn and Quinlan 2018) and randomForests (Liaw and Wiener 2002).

Calibrated models were used to predict for the validation dataset, and prediction statistics, including root mean squared error (RMSE), coefficient of determination (R^2),

Bias, Accuracy, and Cohen's kappa coefficient (Kappa) were calculated to evaluate model performance. RMSE indicates the average prediction error compared to the observations. R^2 indicates the percentage of observation variance that is explained by the model. Bias indicates the average prediction deviation from the observations. Accuracy indicates the percentage of overall accurate classifications. Kappa indicates the agreement between observed and predicted classes. The statistics were defined as the following:

$$RMSE = \sqrt{\frac{1}{n}\sum_i (P_i - O_i)^2}, \tag{4.20}$$

$$R^2 = 1 - \frac{\sum_i (O_i - P_i)^2}{\sum_i (O_i - \bar{O})^2}, \tag{4.21}$$

$$Bias = \frac{1}{n}\sum_i (P_i - O_i), \tag{4.22}$$

$$Accuracy = \frac{c}{n}, \tag{4.23}$$

$$Kappa = \frac{Accuracy - E}{1 - E}, \tag{4.24}$$

where n is the number of observations or the number of data entries of the validation dataset, P_i is the ith prediction, O_i is the ith observation, $\bar{O}$ is the mean of observations, and c is the number of correct classifications. Notice n was different for each soybean trait because of the data availability (Table 4.3). E is defined as:

$$E = \frac{1}{n^2}\sum_k np_k no_k, \tag{4.25}$$

where k is the kth class, np_k is the number of predictions in kth class, no_k is the number of observations in kth class.

4.4. Results

When using all 457 variables as predictor variables, Cubist as the regression technique, and Random Forests as the classification technique, prediction results for all soybean traits were presented below (Figure 4.7). Aside from the statistics showing in the figure, Lodging had an Accuracy of 0.7662 and a Kappa of 0.3910, and Seed Quality had an Accuracy of 0.6629 and a Kappa of 0.1687.

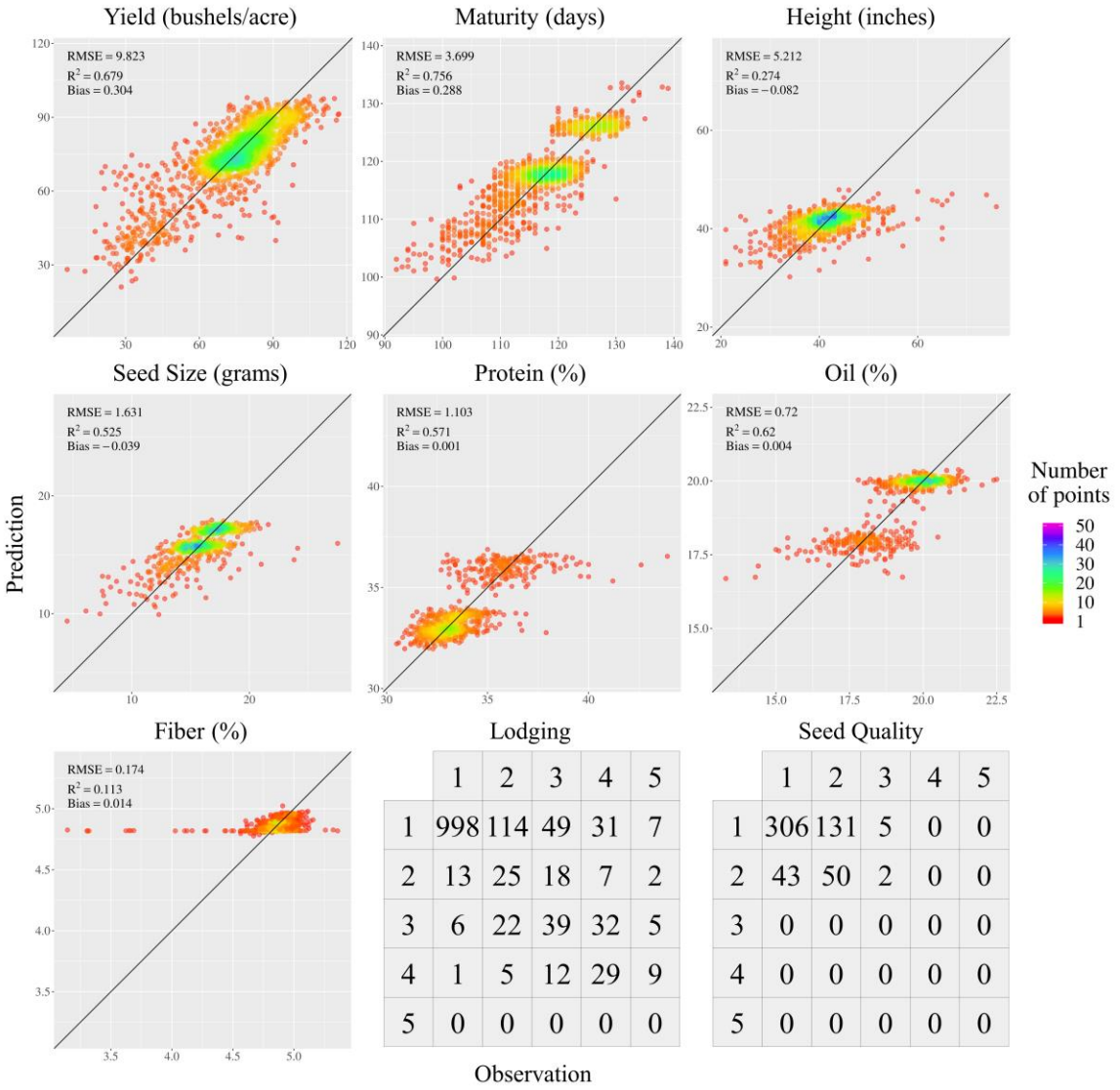

	1	2	3	4	5
1	998	114	49	31	7
2	13	25	18	7	2
3	6	22	39	32	5
4	1	5	12	29	9
5	0	0	0	0	0

	1	2	3	4	5
1	306	131	5	0	0
2	43	50	2	0	0
3	0	0	0	0	0
4	0	0	0	0	0
5	0	0	0	0	0

Figure 4.7. Prediction results for all soybean traits using all 457 predictor variables.

Statistically speaking, Seed Size, Protein, Oil and Fiber had very small RMSEs, Yield and Maturity had fair RMSEs, and Height had a large RMSE. Yield, Maturity, Seed Size, Protein and Oil all had decent R^2s, whereas Height and Fiber had low R^2s indicating models were not able to explain large percentages of the data variances. All soybean traits had very small Biases. Both Lodging and Seed Quality had good prediction Accuracy, however their Kappa were very low. The reason that caused this phenomenon might be the imbalanced data distribution, meaning Lodging and Seed Quality had large proportions of low rating scores, whereas only a few high rating scores existed. In this scenario even if a model classifies all data entries as low rating, Accuracy of the result can still be high.

Data clusters were observed in Maturity, Seed Size, Protein and Oil. When compared to the rest three locations, Clay Center had the highest overall Maturity distribution, and the cluster at upper right corner in Maturity represented the soybean plots influenced by Clay Center's location effect. Similar to Maturity, clusters in Seed Size also indicated location difference. The Seed Size distributions of Cotesfield and Wymore were centered around 17 while Clay Center and Mead were centered around 15, thus each of the two clusters in Seed Size represented two locations. The clusters in Protein and Oil showed difference in between soybean populations. The cluster at upper right corner in Protein and the cluster at lower left corner in Oil represented the same soybean population, which was developed for improved genotype diversity. All other soybean populations behaved similarly in Protein and Oil.

Based on the overall consideration of the prediction results, we identified Yield,

Maturity and Seed Size as the potential soybean traits for early prediction purpose.

4.5. Discussion

4.5.1. Agronomical Interpretation

Our results suggested that several end-season soybean traits might be predictable through the color and texture feature of early-season canopy images. Since this subject has never been explored before, the true reason for the results remained unknown. Ushada et al. (2007) estimated moss traits through GLCM-based canopy texture features, and they proposed a black box relationship between canopy parameters and canopy image. Here we proposed several theoretical explanations in an attempt to connect plant parameters and color and texture features of canopy images.

Plant developmental traits, such as plant architecture and leaf features, are important factors that determine plant overall performance, which can be reflected in an early-season canopy image. It is logical to assume the color and texture features of a crop canopy image indicate, or represent crop parameters as well as the interactions between the parameters. We identified five major crop parameters below that are represented by the color and texture information of a canopy image. In other words, the variation of the color and texture indices of a canopy image is mainly affected by the following five plant developmental parameters:

- Leaf color

Plant leaf color is associated with biotic and abiotic stresses, such as plant diseases (Matsunaga et al. 2017) and nutrient deficiencies (Xu et al. 2011), which

typically cause chlorophyll destruction or chlorophyll formation failure. A common practice in crop nitrogen management is to use a leaf color chart, which utilizes relative leaf greenness as an indicator for leaf nitrogen status. A healthy plant leaf should have a uniform green color distribution, and the corresponding canopy RGB image should have small standard deviations in all three channels. A diseased leaf may have necrotic lesions with non-green colors, which leads to larger standard deviations in all channels because of the nonuniform color distribution. Nutrient deficient or drought-stressed leaves often have chlorosis, which can lead to shifts of means in three channels. Essentially leaf color indicates plant vigor and health, and it is reasonable to imagine vigorous young plants can have better performance later on.

- Leaf shape

Plants with different genotypes can have diverse leaf shapes, which can further influence the efficiency of light harvesting when leaf area density is high. From the perspective of a 2D image, leaf shape is also affected by leaf or branch angle, which has a heavy effect on the amount light that can be received by the leaf. Though it was not observed in our images, insect damage, plant disease or environmental stress can also change the shape of leaf. In relation to canopy RGB imagery, texture indices are apparently affected by the shape of leaves since leaves are the fundamental subunits that give the overall canopy texture appearance. Leaf shape contains the information regarding plant health and photosynthetic efficiency, thus is partially responsible for plant end-season performance.

• Leaf Size

Since our images were all collected at the same growth stage, the leaf size difference between plots could indicate plant growth rates. Also leaf size is directly related with cell number and chlorophyll content, which in turn determine plant photosynthetic capacity (Mathan, Bhattacharya, and Ranjan 2016). Both plant growth rate and photosynthetic capacity have been found to be correlated with yield (Ashraf and Bashir 2003; Matsuo et al. 2018). Large leaf size can give canopy a "coarser" texture appearance, while small leaf size gives a "finer" canopy appearance. This appearance difference would eventually affects the values of texture indices.

• Leaf Area Density

Leaf area density describes how dense the leaves distribute spatially. Similar to leaf angle and leaf size, leaf area density directly influences plant photosynthetic capacity and the quantity of light interception, therefore leaf photosynthetic efficiency is influenced, which in the long-term can have a substantial accumulated effect on plant end-season performance. Also leaf area density indirectly shows the number of stems or branches, which is usually negatively correlated with plant height and lodging. High leaf area density can add complexity to plant canopy texture, while canopies with low leaf area density would have a "simpler" appearance.

• Plant Density

As the seeding rates for all soybean plots that we measured were the same, plant density showing in the images indicated the germination rate of a plot. Also plant density

interferes plant photosynthetic efficiency by affecting the quantity of light interception. It is logical to expect a plot with fewer plants emerged to have less final yield.

The color and texture indices of an early-season canopy image statistically represent various characteristics of a plant, such as leaf color, leaf shape, leaf angle, branch angle, leaf size, plant growth rate, leaf area density, stem number, branch number, germination rate, etc. These plant developmental parameters further indicate or determine plant vigor, plant health, plant photosynthetic efficiency, plant photosynthetic capacity, plant drought resistance, etc. at early growth stages, which can have significant influence on plant overall performance (Figure 7).

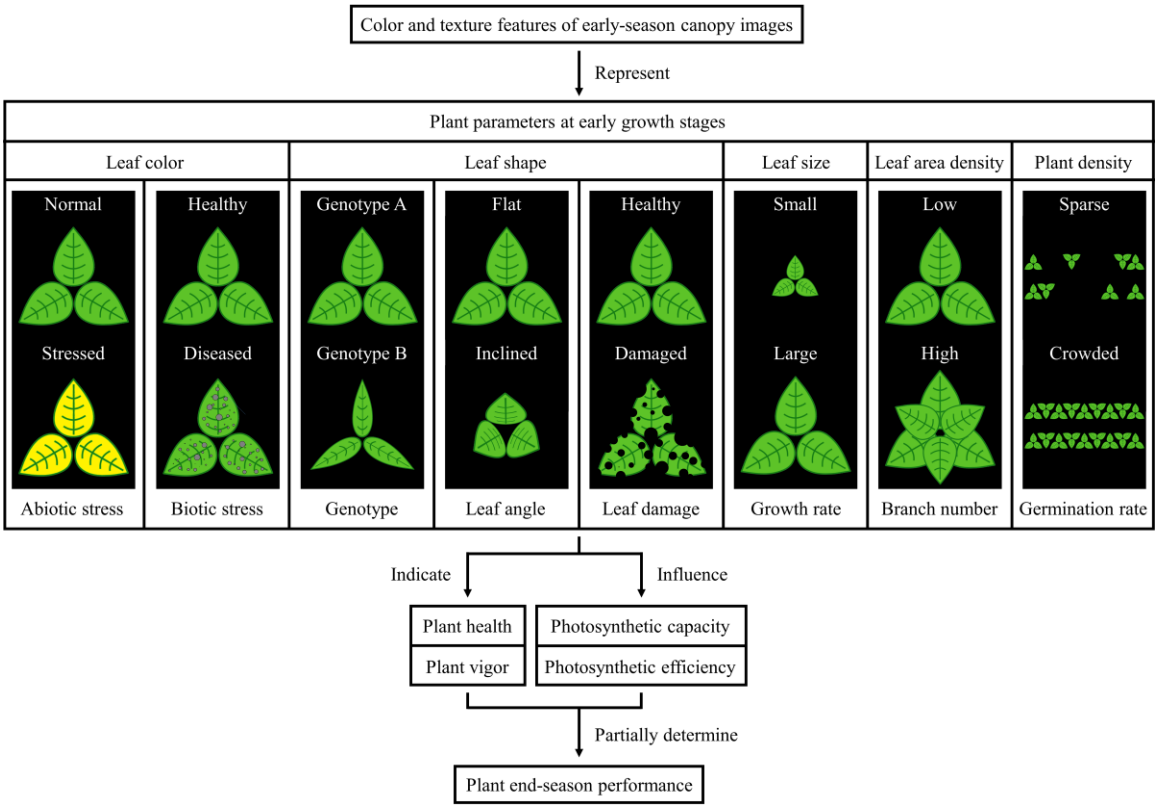

Figure 4.8. Schematic diagram explaining the potential relationships between color and texture information of early-season canopy images and end-season plant performance.

4.5.2. Limitations of the Study and Directions for Future Studies

An image is often rescaled into fewer gray levels before calculating its GLCMs. However, assuming the more gray levels there are the more information an image contains, we chose 256 gray levels for our transformed image dataset. Research has found that the classification ability of some texture indices decreases when the number of gray levels increases (Clausi 2002). Future studies can investigate the optimal gray level quantization for crop trait early prediction purpose by rescaling images into 128, 64, 32, 16 or 8 gray levels and comparing the predictions results. Optimal pixel displacement can be explored in a similar manner. Also, instead of only computing GLCMs of two scanning directions, GLCMs of all four scanning directions can be computed and their texture indices can be averaged as more comprehensive representations of a canopy.

A flaw in our image dataset was that the images were not color-calibrated. Image color is subject to the lighting condition, which can cause inconsistent color representations across images, that is, the same pixel value intensity can represent different colors in different images. One common method for image color calibration is to capture a camera calibration target in all images, such as ColorChecker (X-Rite, Grand Rapids, MI, USA) (Sunoj et al. 2018). Yet, how to effectively implement a calibration target into a high-throughput phenotyping system when measuring thousands of plots remains a challenge for future research.

The cameras employed in this study were not able to capture the fine vasculature of soybean leaves. Vasculature features such as vein density and vein diameter regulate plant mechanical strength and serve as channels for transporting nutrients such as water

and minerals (Mathan et al. 2016), therefore they are crucial for plant photosynthesis. If the images have sufficient spatial resolutions to capture leaf vasculature, texture indices can be good indicators for subtle leaf vasculature difference.

The soybean image dataset in this study was collected at eastern Nebraska areas in the year of 2016. Without images collected over a different crop type, from another location with different environmental conditions, or from another year as reference, significant crop, location, year effects on plant end-season performance might exist. Thus, all conclusions made in this article are solely valid for soybean plots growing at eastern Nebraska in 2016 and cannot be generalized. As the concept of this study is rudimentary, experiments for various crops under diverse environments across multiple years are needed to confirm the validity and applicability of crop trait early prediction through RGB imagery.

4.6. Conclusion

Based on the results of this study, Yield, Maturity and Seed Size are the soybean traits that might be predictable using color and texture features of early-season canopy RGB images. However this conclusion is only valid for soybean growing at eastern Nebraska in 2016, and the concept of crop trait early prediction needs future studies to consolidate.

REFERENCES

Al-Saddik, Hania, Anthony Laybros, Bastien Billiot, and Frederic Cointault. 2018. "Using Image Texture and Spectral Reflectance Analysis to Detect Yellowness and Esca in Grapevines at Leaf-Level." *Remote Sensing* 10(4).

Andrade-Sanchez, Pedro, Michael A. Gore, John T. Heun, Kelly R. Thorp, A. Elizabete Carmo-Silva, Andrew N. French, Michael E. Salvucci, and Jeffrey W. White. 2014. "Development and Evaluation of a Field-Based , High-Thoughput Phenotyping Platform." *Functional Plant Biology* 41(September 2015):68–79.

Andújar, Dionisio, Martin Weis, and Roland Gerhards. 2012. "An Ultrasonic System for Weed Detection in Cereal Crops." *Sensors* 12(12):17343–57.

Anys, Hassan and Dong-Chen He. 1995. "Evaluation of Textural and Multipolarization Radar Features for Crop Classification." *IEEE Transactions on Geoscience and Remote Sensing* 33(5):1170–81.

Aquino, Arturo, Borja Millan, Maria-Paz Diago, and Javier Tardaguila. 2018. "Automated Early Yield Prediction in Vineyards from On-the-Go Image Acquisition." *Computers and Electronics in Agriculture* 144:26–36.

Araus, José Luis, Shawn C. Kefauver, Mainassara Zaman-Allah, Mike S. Olsen, and Jill E. Cairns. 2018. "Translating High-Throughput Phenotyping into Genetic Gain." *Trends in Plant Science* 23(5):451–66.

Ashraf, M. and Alweena Bashir. 2003. "Relationship of Photosynthetic Capacity at the Vegetative Stage and during Grain Development with Grain Yield of Two Hexaploid Wheat (Triticum Aestivum L.) Cultivars Differing in Yield." *European Journal of Agronomy* 19(2):277–87.

Bai, Geng, Yufeng Ge, Waseem Hussain, P. Stephen Baenziger, and George Graef. 2016. "A Multi-Sensor System for High Throughput Field Phenotyping in Soybean and Wheat Breeding." *Computers and Electronics in Agriculture* 128:181–92.

Bai, Geng, Shawn Jenkins, Wenan Yuan, George L. Graef, and Yufeng Ge. 2018. "Field-Based Scoring of Soybean Iron Deficiency Chlorosis Using RGB Imaging and Statistical Learning." *Frontiers in Plant Science* 9:1002.

Bakhshipour, Adel, Abdolabbas Jafari, and Farahmand Babellahi. 2013. "Using of Artificial Intelligence and Image Texture to Estimate Desiccation Rate of Quince Fruit." *Technical Journal of Engineering and Applied Sciences* 3(7):641–46.

Balota, Maria, William A. Payne, Steven R. Evett, and Mark D. Lazar. 2007. "Canopy Temperature Depression Sampling to Assess Grain Yield and Genotypic Diff Erentiation in Winter Wheat." *Crop Science* 47(4):1518–29.

Barker, Jared III, Naiqian Zhang, Joshua Sharon, Ryan Steeves, Xu Wang, Yong Wei, and Jesse Poland. 2016. "Development of a Field-Based High-Throughput Mobile Phenotyping Platform." *Computers and Electronics in Agriculture* 122:74–85.

Barmeier, Gero, Bodo Mistele, and Urs Schmidhalter. 2016. "Referencing Laser and Ultrasonic Height Measurements of Barleycultivars by Using a Herbometre as Standard." *Crop and Pasture Science* 67(12):1215–22.

Barrero, Oscar, Diana Rojas, Christian Gonzalez, and Sammy Perdomo. 2016. "Weed Detection in Rice Fields Using Aerial Images and Neural Networks." Pp. 1–4 in *2016 XXI Symposium on Signal Processing, Images and Artificial Vision (STSIVA)*. IEEE.

Behjati, Sam and Patrick S. Tarpey. 2013. "What Is next Generation Sequencing?" *Archives of Disease in Childhood: Education and Practice Edition* 98(6):236–38.

Beliakov, Gleb, Simon James, and Luigi Troiano. 2008. "Texture Recognition by Using GLCM and Various Aggregation Functions." Pp. 1472–76 in *2008 IEEE International Conference on Fuzzy Systems*.

Bendig, Juliane, Kang Yu, Helge Aasen, Andreas Bolten, Simon Bennertz, Janis Broscheit, Martin L. Gnyp, and Georg Bareth. 2015. "Combining UAV-Based Plant Height from Crop Surface Models, Visible, and near Infrared Vegetation Indices for Biomass Monitoring in Barley." *International Journal of Applied Earth Observation and Geoinformation* 39:79–87.

Bharati, Manish H., J. Jay Liu, and John F. MacGregor. 2004. "Image Texture Analysis: Methods and Comparisons." *Chemometrics and Intelligent Laboratory Systems* 72:57–71.

Bhatta, Madhav, Kent M. Eskridge, Devin J. Rose, Dipak K. Santra, P. Stephen Baenziger, and Teshome Regassa. 2017. "Seeding Rate, Genotype, and Topdressed Nitrogen Effects on Yield and Agronomic Characteristics of Winter Wheat." *Crop Science* 57(2):951–63.

Burgos-Artizzu, Xavier P., Angela Ribeiro, Maria Guijarro, and Gonzalo Pajares. 2011. "Real-Time Image Processing for Crop/Weed Discrimination in Maize Fields." *Computers and Electronics in Agriculture* 75:337–46.

Busemeyer, Lucas, Daniel Mentrup, Kim Möller, Erik Wunder, Katharina Alheit, Volker

Hahn, Hans Peter Maurer, Jochen C. Reif, Tobias Würschum, Joachim Müller, Florian Rahe, and Arno Ruckelshausen. 2013. "BreedVision — A Multi-Sensor Platform for Non-Destructive Field-Based Phenotyping in Plant Breeding." *Sensors* 13(3):2830–47.

Casadesús, J., Y. Kaya, J. Bort, M. M. Nachit, J. L. Araus, S. Amor, G. Ferrazzano, F. Maalouf, M. Maccaferri, V. Martos, H. Ouabbou, and D. Villegas. 2007. "Using Vegetation Indices Derived from Conventional Digital Cameras as Selection Criteria for Wheat Breeding in Water-Limited Environments." *Annals of Applied Biology* 150(2):227–36.

Chaki, Jyotismita, Ranjan Parekh, and Samar Bhattacharya. 2015. "Plant Leaf Recognition Using Texture and Shape Features with Neural Classifiers." *Pattern Recognition Letters* 58:61–68.

Chang, Y. K., Q. U. Zaman, A. W. Schumann, D. C. Percival, T. J. Esau, and G. Ayalew. 2012. "Development of Color Co-Occurrence Matrix Based Machine Vision Algorithms for Wild Blueberry Fields." *Applied Engineering in Agriculture* 28(3):315–23.

Chang, Young K., Qamar U. Zaman, Tanzeel U. Rehman, Aitazaz A. Farooque, Travis Esau, and Muhammad W. Jameel. 2017. "A Real-Time Ultrasonic System to Measure Wild Blueberry Plant Height during Harvesting." *Biosystems Engineering* 157:35–44.

Chaudhary, Piyush, Anand K. Chaudhari, A. N. Cheeran, and Sharda Godara. 2012. "Color Transform Based Approach for Disease Spot Detection on Plant Leaf." *International Journal of Computer Science and Telecommunications* 3(6):65–71.

Clausi, David A. 2002. "An Analysis of Co-Occurrence Texture Statistics as a Function of Grey Level Quantization." *Canadian Journal of Remote Sensing* 28(1):45–62.

Conners, Richard W. and Charles A. Harlow. 1980. "A Theoretical Comparison of Texture Algorithms." *IEEE Transactions on Pattern Analysis and Machine Intelligence* PAMI-2(3):204–22.

Deery, David, Jose Jimenez-Berni, Hamlyn Jones, Xavier Sirault, and Robert Furbank. 2014. *Proximal Remote Sensing Buggies and Potential Applications for Field-Based Phenotyping*. Vol. 4.

Delwiche, Stephen R., I. Chang Yang, and Robert A. Graybosch. 2013. "Multiple View Image Analysis of Freefalling U.S. Wheat Grains for Damage Assessment." *Computers and Electronics in Agriculture* 98:62–73.

Dorigo, Wouter, Arko Lucieer, Tomaž Podobnikar, and Andraž Carni. 2012. "Mapping Invasive Fallopia Japonica by Combined Spectral, Spatial, and Temporal Analysis of Digital Orthophotos." *International Journal of Applied Earth Observation and Geoinformation* 19(1):185–95.

Du, Mengmeng and Noboru Noguchi. 2017. "Monitoring of Wheat Growth Status and Mapping of Wheat Yield's within-Field Spatial Variations Using Color Images Acquired from UAV-Camera System." *Remote Sensing* 9(3).

Elibox, Winston. 2012. "Early Prediction of Juice Brix and Associated Fibre Content at Maturity in Sugarcane (Saccharum Spp. Hybrids) Cultivated in Barbados." *International Sugar Journal* 114(1368):886–93.

Farooque, Aitazaz A., Young K. Chang, Qamar U. Zaman, Dominic Groulx, Arnold W. Schumann, and Travis J. Esau. 2013. "Performance Evaluation of Multiple Ground Based Sensors Mounted on a Commercial Wild Blueberry Harvester to Sense Plant Height, Fruit Yield and Topographic Features in Real-Time." *Computers and Electronics in Agriculture* 91:135–44.

Fricke, Thomas, Felix Richter, and Michael Wachendorf. 2011. "Assessment of Forage Mass from Grassland Swards by Height Measurement Using an Ultrasonic Sensor." *Computers and Electronics in Agriculture* 79(2):142–52.

Fricke, Thomas and Michael Wachendorf. 2013. "Combining Ultrasonic Sward Height and Spectral Signatures to Assess the Biomass of Legume-Grass Swards." *Computers and Electronics in Agriculture* 99:236–47.

Friedli, Michael, Norbert Kirchgessner, Christoph Grieder, Frank Liebisch, Michael Mannale, and Achim Walter. 2016. "Terrestrial 3D Laser Scanning to Track the Increase in Canopy Height of Both Monocot and Dicot Crop Species under Field Conditions." *Plant Methods* 12(1):1–15.

Gao, Junfeng, Xiaoli Li, Fengle Zhu, and Yong He. 2013. "Application of Hyperspectral Imaging Technology to Discriminate Different Geographical Origins of Jatropha Curcas L. Seeds." *Computers and Electronics in Agriculture* 99:186–93.

Guevara-Hernandez, F. and J. Gomez-Gil. 2011. "A Machine Vision System for Classification of Wheat and Barley Grain Kernels." *Spanish Journal of Agricultural Research* 9(3):672.

Guijarro, M., G. Pajares, I. Riomoros, P. J. Herrera, X. P. Burgos-Artizzu, and A. Ribeiro. 2011. "Automatic Segmentation of Relevant Textures in Agricultural Images." *Computers and Electronics in Agriculture* 75(1):75–83.

Hamuda, Esmael, Martin Glavin, and Edward Jones. 2016. "A Survey of Image Processing Techniques for Plant Extraction and Segmentation in the Field." *Computers and Electronics in Agriculture* 125:184–99.

Han, Wenting, Yu Sun, Tengfei Xu, Xiangwei Chen, and Ki Ooi Su. 2014. "Detecting Maize Leaf Water Status by Using Digital RGB Images." *International Journal of Agricultural and Biological Engineering* 7(1):45–53.

Haralick, Robert M., K. Shanmugam, and Its'hak Dinstein. 1973. "Textural Features for Image Classification." *IEEE Transactions on Systems, Man and Cybernetics* SMC-3(6):610–21.

Huang, Kuo-Yi. 2007. "Application of Artificial Neural Network for Detecting Phalaenopsis Seedling Diseases Using Color and Texture Features." *Computers and Electronics in Agriculture* 57:3–11.

Hunt, E. Raymond Jr., Michel Cavigelli, Craig S. T. Daughtry, James III McMurtrey, and Charles L. Walthall. 2005. "Evaluation of Digital Photography from Model Aircraft for Remote Sensing of Crop Biomass and Nitrogen Status." *Precision Agriculture* 6(4):359–78.

Hunt, E. Raymond Jr., C. S. T. Daughtry, Jan U. H. Eitel, and Dan S. Long. 2011. "Remote Sensing Leaf Chlorophyll Content Using a Visible Band Index." *Agronomy Journal* 103(4):1090–99.

Hunt, E. Raymond Jr., Paul C. Doraiswamy, James E. McMurtrey, Craig S. T. Daughtry, Eileen M. Perry, and AkhmedovBakhyt. 2013. "A Visible Band Index for Remote Sensing Leaf Chlorophyll Content at the Canopy Scale." *International Journal of Applied Earth Observation and Geoinformation* 21:103–12.

Jackson, R. D., S. B. Idso, R. J. Reginato, and P. J. Jr. Pinter. 1981. "Canopy Temperature as a Crop Water Stress Indicator." *Water Resources Research* 17(4):1133–38.

Jackson, R. D., R. J. Reginato, and S. B. Idso. 1977. "Wheat Canopy Temperature: A Practical Tool for Evaluating Water Requirements." *Water Resources Research* 13(3):651–56.

Jiang, Boran, Ping Wang, Shuo Zhuang, Maosong Li, Zhenfa Li, and Zhihong Gong. 2018. "Detection of Maize Drought Based on Texture and Morphological Features." *Computers and Electronics in Agriculture* 151:50–60.

Jimenez-Berni, Jose A., David M. Deery, Pablo Rozas-Larraondo, Anthony (Tony) G. Condon, Greg J. Rebetzke, Richard A. James, William D. Bovill, Robert T.

Furbank, and Xavier R. R. Sirault. 2018. “High Throughput Determination of Plant Height, Ground Cover, and Above-Ground Biomass in Wheat with LiDAR.” *Frontiers in Plant Science* 9(February):1–18.

Kadir, Abdul. 2014. “A Model of Plant Identification System Using GLCM, Lacunarity And Shen Features Abdul.” *Research Journal of Pharmaceutical, Biological and Chemical Sciences* 5(2):1–10.

Karcher, Douglas E. and Michael D. Richardson. 2003. “Quantifying Turfgrass Color Using Digital Image Analysis.” *Crop Science* 43(3):943–51.

Kataoka, Takashi, Toshihiro Kaneko, Hiroshi Okamoto, and Shun-ichi Hata. 2003. “Crop Growth Estimation System Using Machine Vision.” Pp. 1079–83 in *Proceedings 2003 IEEE/ASME International Conference on Advanced Intelligent Mechatronics (AIM 2003)*.

Kaya, Yilmaz, Mehmet Emre Erez, Osman Karabacak, Lokman Kayci, and Mehmet Fidan. 2013. “An Automatic Identification Method for the Comparison of Plant and Honey Pollen Based on GLCM Texture Features and Artificial Neural Network.” *Grana* 52(1):71–77.

Kayitakire, F., C. Hamel, and P. Defourny. 2006. “Retrieving Forest Structure Variables Based on Image Texture Analysis and IKONOS-2 Imagery.” *Remote Sensing of Environment* 102(3–4):390–401.

Kuhn, Max and Ross Quinlan. 2018. “Cubist: Rule- And Instance-Based Regression Modeling.”

Leemans, Vincent, Guillaume Marlier, Marie-France Destain, Benjamin Dumont, and Benoit Mercatoris. 2017. “Estimation of Leaf Nitrogen Concentration on Winter Wheat by Multispectral Imaging.” Pp. 102130I-10213–10 in *Proc. SPIE 10213, Hyperspectral Imaging Sensors: Innovative Applications and Sensor Standards 2017*. Vol. 10213.

Li, Huihui, Awais Rasheed, Lee T. Hickey, and Zhonghu He. 2018. “Fast-Forwarding Genetic Gain.” *Trends in Plant Science* 23(3):184–86.

Liaw, Andy and Matthew Wiener. 2002. “Classification and Regression by RandomForest.” *R News* 2(3):18–22.

Liu, Tian-Hu, Reza Ehsani, Arash Toudeshki, Xiang-Jun Zou, and Hong-Jun Wang. 2018. “Identifying Immature and Mature Pomelo Fruits in Trees by Elliptical Model Fitting in the Cr–Cb Color Space.” *Precision Agriculture* 20(1):138–56.

López-Lapeña, Oscar and Ramon Pallas-Areny. 2018. “Solar Energy Radiation Measurement with a Low–Power Solar Energy Harvester.” *Computers and Electronics in Agriculture* 151(February):150–55.

Louhaichi, Mounir, Michael M. Borman, and Douglas E. Johnson. 2001. “Spatially Located Platform and Aerial Photography for Documentation of Grazing Impacts on Wheat.” *Geocarto International* 16(1):65–70.

Ma, B. L., Lianne M. Dwyer, Carlos Costa, Elroy R. Cober, and Malcolm J. Morrison. 2001. “Early Prediction of Soybean Yield from Canopy Reflectance Measurements.” *Agronomy Journal* 93(6):1227–34.

Madec, Simon, Fred Baret, Benoît de Solan, Samuel Thomas, Dan Dutartre, Stéphane Jezequel, Matthieu Hemmerlé, Gallian Colombeau, and Alexis Comar. 2017. “High-Throughput Phenotyping of Plant Height: Comparing Unmanned Aerial Vehicles and Ground LiDAR Estimates.” *Frontiers in Plant Science* 8:1–14.

Majumdar, Diptesh, Dipak Kumar Kole, Aruna Chakraborty, and Dwijesh Dutta Majumder. 2015. “An Integrated Digital Image Analysis System for Detection, Recognition and Diagnosis of Disease in Wheat Leaves.” Pp. 400–405 in *Proceedings of the Third International Symposium on Women in Computing and Informatics*.

Majumdar, S. and D. S. Jayas. 2000. “Classification of Cereal Grains Using Machine Vision: III. Texture Models.” *Transactions of the ASAE* 43(6):1681–87.

Mao, Shuang-Lin, Yu-Ming Wei, Wenguang Cao, Xiu-Jin Lan, Ma Yu, Zheng-Mao Chen, Guo-Yue Chen, and You-Liang Zheng. 2010. “Confirmation of the Relationship between Plant Height and Fusarium Head Blight Resistance in Wheat (Triticum Aestivum L.) by QTL Meta-Analysis.” *Euphytica* 174(3):343–56.

Materka, Andrzej and Michal Strzelecki. 1998. *Texture Analysis Methods – A Review*.

Mathan, Jyotirmaya, Juhi Bhattacharya, and Aashish Ranjan. 2016. “Enhancing Crop Yield by Optimizing Plant Developmental Features.” *Development* 143(18):3283–94.

Matsunaga, Tomoko M., Daisuke Ogawa, Fumio Taguchi-Shiobara, Masao Ishimoto, Sachihiro Matsunaga, and Yoshiki Habu. 2017. “Direct Quantitative Evaluation of Disease Symptoms on Living Plant Leaves Growing under Natural Light.” *Breeding Science* 67(3):316–19.

Matsuo, Naoki, Tetsuya Yamada, Yoshitake Takada, Koichiro Fukami, and Makita Hajika. 2018. “Effect of Plant Density on Growth and Yield of New Soybean

Genotypes Grown under Early Planting Condition in Southwestern Japan." *Plant Production Science* 21(1):16–25.

Meyer, George E., Timothy W. Hindman, and Koppolu Laksmi. 1999. "Machine Vision Detection Parameters for Plant Species Identification." in *Proc.SPIE*. Vol. 3543.

Meyer, George E. and João Camargo Neto. 2008. "Verification of Color Vegetation Indices for Automated Crop Imaging Applications." *Computers and Electronics in Agriculture* 63(2):282–93.

Nasir, A. Fakhri A., M. Nordin A. Rahman, Nashriyah Mat, and A. Rasid Mamat. 2014. "Automatic Identification of Ficus Deltoidea Jack (Moraceae) Varieties Based on Leaf." *Modern Applied Science* 8(5):121–31.

Navabi, A., M. Iqbal, K. Strenzke, and D. Spaner. 2006. "The Relationship between Lodging and Plant Height in a Diverse Wheat Population." *Canadian Journal of Plant Science* 86(3):723–26.

Otsu, Nobuyuki. 1979. "A Threshold Selection Method from Gray-Level Histograms." *IEEE Transactions on Systems, Man, and Cybernetics* 9(1):62–66.

Pittman, Jeremy Joshua, Daryl Brian Arnall, Sindy M. Interrante, Corey A. Moffet, and Twain J. Butler. 2015. "Estimation of Biomass and Canopy Height in Bermudagrass, Alfalfa, and Wheat Using Ultrasonic, Laser, and Spectral Sensors." *Sensors* 15(2):2920–43.

Pujari, Jagadeesh D., Rajesh Yakkundimath, and Abdulmunaf S. Byadgi. 2014. "Recognition and Classification of Produce Affected by Identically Looking Powdery Mildew Disease." *Acta Technologica Agriculturae* 17(2):29–34.

Pulido, Camilo, Leonardo Solaque, and Nelson Velasco. 2017. "Weed Recognition by SVM Texture Feature Classification in Outdoor Vegetable Crops Images." *Ingeniería e Investigación* 37(1):68–74.

R Core Team. 2018. "R: A Language and Environment for Statistical Computing."

Ray, Deepak K., Nathaniel D. Mueller, Paul C. West, and Jonathan A. Foley. 2013. "Yield Trends Are Insufficient to Double Global Crop Production by 2050." *PLoS ONE* 8(6).

Ray, Deepak K., Navin Ramankutty, Nathaniel D. Mueller, Paul C. West, and Jonathan A. Foley. 2012. "Recent Patterns of Crop Yield Growth and Stagnation." *Nature Communications* 3:1293–97.

Ritchie, G. L., D. G. Sullivan, W. K. Vencill, C. W. Bednarz, and J. E. Hook. 2010. "Sensitivities of Normalized Difference Vegetation Index and a Green/Red Ratio Index to Cotton Ground Cover Fraction." *Crop Science* 50(3):1000–1010.

Rusu, Radu Bogdan, Zoltan Csaba Marton, Nico Blodow, Mihai Dolha, and Michael Beetz. 2008. "Towards 3D Point Cloud Based Object Maps for Household Environments." *Robotics and Autonomous Systems* 56(11):927–41.

Saa, Sebastian, Patrick H. Brown, Saiful Muhammad, Andres Olivos-Del Rio, Blake L. Sanden, and Emilio A. Laca. 2014. "Prediction of Leaf Nitrogen from Early Season Samples and Development of Field Sampling Protocols for Nitrogen Management in Almond (Prunus Dulcis [Mill.] DA Webb)." *Plant and Soil* 380(1):153–63.

Sanjerehei, Mohammad Mousaei. 2014. "Assessment of Spectral Vegetation Indices for Estimating Vegetation Cover in Arid and Semiarid Shrublands." *Range Management and Agroforestry* 35(1):91–100.

Sarker, Latifur Rahman and Janet E. Nichol. 2011. "Improved Forest Biomass Estimates Using ALOS AVNIR-2 Texture Indices." *Remote Sensing of Environment* 115(4):968–77.

Schirrmann, Michael, André Hamdorf, Andreas Garz, Anton Ustyuzhanin, and Karl Heinz Dammer. 2016. "Estimating Wheat Biomass by Combining Image Clustering with Crop Height." *Computers and Electronics in Agriculture* 121:374–84.

Scotford, I. M. and P. C. H. Miller. 2004. "Combination of Spectral Reflectance and Ultrasonic Sensing to Monitor the Growth of Winter Wheat." *Biosystems Engineering* 87(1):27–38.

Sharma, Bablu and Glen L. Ritchie. 2015. "High-Throughput Phenotyping of Cotton in Multiple Irrigation Environments." *Crop Science* 55(2):958–69.

Shearer, S. A. and R. G. Holmes. 1990. "Plant Identification Using Color Co-Occurrence Matrices." *Transactions of the ASAE* 33(6):2037–2044.

Shi, Y., N. Wang, R. K. Taylor, and W. R. Raun. 2015. "Improvement of a Ground-LiDAR-Based Corn Plant Population and Spacing Measurement System." *Computers and Electronics in Agriculture* 112:92–101.

Shimada, S., J. Matsumoto, A. Sekiyama, B. Aosier, and M. Yokohana. 2012. "A New Spectral Index to Detect Poaceae Grass Abundance in Mongolian Grasslands." *Advances in Space Research* 50(9):1266–73.

Siraj, Fadzilah, Hawa Mohd Ekhsan, and Abdul Nasir Zulkifli. 2014. "Flower Image Classification Modeling Using Neural Network." Pp. 81–86 in *2014 International Conference on Computer, Control, Informatics and Its Applications (IC3INA)*. IEEE.

Stroup, Walter W., P. Stephen Baenziger, and Dieter K. Mulitze. 1994. "Removing Spatial Variation from Wheat Yield Trials: A Comparison of Methods." *Crop Science* 34(1):62–66.

Sun, Shangpeng and Changying Li. 2016. "Height Estimation for Blueberry Bushes Using LiDAR Based on a Field Robotic Platform." Pp. 2–12 in *2016 ASABE Annual International Meeting*.

Sun, Shangpeng, Changying Li, and Andrew H. Paterson. 2017. "In-Field High-Throughput Phenotyping of Cotton Plant Height Using LiDAR." *Remote Sensing* 9(4):1–21.

Sunoj, S., C. Igathinathane, N. Saliendra, J. Hendrickson, and D. Archer. 2018. "Color Calibration of Digital Images for Agriculture and Other Applications." *ISPRS Journal of Photogrammetry and Remote Sensing* 146(June):221–34.

Tester, Mark and Peter Langridge. 2010. "Breeding Technologies to Increase Crop Production in a Changing World." *Science* 327(5967):818–22.

Tilman, David, Christian Balzer, Jason Hill, and Belinda L. Befort. 2011. "Global Food Demand and the Sustainable Intensification of Agriculture." *Proceedings of the National Academy of Sciences* 108(50):20260–64.

Tsai, Fuan and Ming-Jhong Chou. 2006. "Texture Augmented Analysis of High Resolution Satellite Imagery in Detecting Invasive Plant Species." *Journal of the Chinese Institute of Engineers* 29(4):581–92.

Underwood, James, Alexander Wendel, Brooke Schofield, Larn McMurray, and Rohan Kimber. 2017. "Efficient In-Field Plant Phenomics for Row-Crops with an Autonomous Ground Vehicle." *Journal of Field Robotics* 34(6):1061–83.

Ushada, M., H. Murase, and H. Fukuda. 2007. "Non-Destructive Sensing and Its Inverse Model for Canopy Parameters Using Texture Analysis and Artificial Neural Network." *Computers and Electronics in Agriculture* 57(2):149–65.

Virlet, Nicolas, Kasra Sabermanesh, Pouria Sadeghi-Tehran, and Malcolm J. Hawkesford. 2017. "Field Scanalyzer: An Automated Robotic Field Phenotyping Platform for Detailed Crop Monitoring." *Functional Plant Biology* 44(1):143–53.

Walter, Achim, Frank Liebisch, and Andreas Hund. 2015. "Plant Phenotyping: From Bean Weighing to Image Analysis." *Plant Methods* 11:1–11.

Wang, Yuan, Dejian Wang, Peihua Shi, and Kenji Omasa. 2014. "Estimating Rice Chlorophyll Content and Leaf Nitrogen Concentration with a Digital Still Color Camera under Natural Light." *Plant Methods* 10(1):36.

Watson, Amy, Sreya Ghosh, Matthew J. Williams, William S. Cuddy, James Simmonds, María Dolores Rey, M. Asyraf Md Hatta, Alison Hinchliffe, Andrew Steed, Daniel Reynolds, Nikolai M. Adamski, Andy Breakspear, Andrey Korolev, Tracey Rayner, Laura E. Dixon, Adnan Riaz, William Martin, Merrill Ryan, David Edwards, Jacqueline Batley, Harsh Raman, Jeremy Carter, Christian Rogers, Claire Domoney, Graham Moore, Wendy Harwood, Paul Nicholson, Mark J. Dieters, Ian H. Delacy, Ji Zhou, Cristobal Uauy, Scott A. Boden, Robert F. Park, Brande B. H. Wulff, and Lee T. Hickey. 2018. "Speed Breeding Is a Powerful Tool to Accelerate Crop Research and Breeding." *Nature Plants* 4(1):23–29.

Wei, Yirong, Liying Chang, Lei Li, Shunkui Ke, Qingliang Niu, and Danfeng Huang. 2012. "Prediction of Sugar Content in Greenhouse Muskmelon Based on Machine Vision." Pp. 173–78 in *4th International Symposium on Models for Plant Growth, Environmental Control and Farm Management in Protected Cultivation*. Vol. 957.

Wilke, Norman, Bastian Siegmann, Lasse Klingbeil, Andreas Burkart, Thorsten Kraska, Onno Muller, Anna van Doorn, Sascha Heinemann, and Uwe Rascher. 2019. "Quantifying Lodging Percentage and Lodging Severity Using a UAV-Based Canopy Height Model Combined with an Objective Threshold Approach." *Remote Sensing* 11(5):515.

Woebbecke, D. M., G. E. Meyer, K. Von Bargen, and D. A. Mortensen. 1995. "Color Indices for Weed Identification Under Various Soil, Residue, and Lighting Conditions." *Transactions of the ASAE* 38(1):259–69.

Wulder, Mike A., Ellsworth F. LeDrew, Steven E. Franklin, and Mike B. Lavigne. 1998. "Aerial Image Texture Information in the Estimation of Northern Deciduous and Mixed Wood Forest Leaf Area Index (LAI)." *Remote Sensing of Environment* 64(1):64–76.

Xie, Chuanqi and Yong He. 2016. "Spectrum and Image Texture Features Analysis for Early Blight Disease Detection on Eggplant Leaves." *Sensors* 16(5).

Xie, Chuanqi, Yongni Shao, Xiaoli Li, and Yong He. 2015. "Detection of Early Blight and Late Blight Diseases on Tomato Leaves Using Hyperspectral Imaging." *Scientific Reports* 5.

Xu, Guili, Fengling Zhang, Syed Ghafoor Shah, Yongqiang Ye, and Hanping Mao. 2011. "Use of Leaf Color Images to Identify Nitrogen and Potassium Deficient Tomatoes." *Pattern Recognition Letters* 32(11):1584–90.

Xu, Rui, Changying Li, and Andrew H. Paterson. 2019. "Multispectral Imaging and Unmanned Aerial Systems for Cotton Plant Phenotyping." *PLOS ONE* 14(2):1–20.

Xue, Jinru and Baofeng Su. 2017. "Significant Remote Sensing Vegetation Indices: A Review of Developments and Applications." *Journal of Sensors* 2017:1–17.

Yalcin, Hulya. 2015. "Phenology Monitoring Of Agricultural Plants Using Texture Analysis." Pp. 338–42 in *2015 4th International Conference on Agro-Geoinformatics*.

Yuan, Wenan, Jiating Li, Madhav Bhatta, Yeyin Shi, P. Stephen Baenziger, and Yufeng Ge. 2018. "Wheat Height Estimation Using LiDAR in Comparison to Ultrasonic Sensor and UAS." *Sensors* 18(11).

Zhang, Xin, Jintian Cui, Weisheng Wang, and Chao Lin. 2017. "A Study for Texture Feature Extraction of High-Resolution Satellite Images Based on a Direction Measure and Gray Level Co-Occurrence Matrix Fusion Algorithm." *Sensors* 17(7).

Zhou, Chengquan, Dong Liang, Xiaodong Yang, Hao Yang, Jibo Yue, and Guijun Yang. 2018. "Wheat Ears Counting in Field Conditions Based on Multi-Feature Optimization and TWSVM." *Frontiers in Plant Science* 9.